ERDC/CRREL TR-00-5

Cold Regions Research and Engineering Laboratory

US Army Corps of Engineers®
Engineer Research and Development Center

UXO Detection at Jefferson Proving Ground Using Ground-Penetrating Radar

Steven A. Arcone, Kevin O'Neill, Allan J. Delaney, and Paul V. Sellmann

April 2000

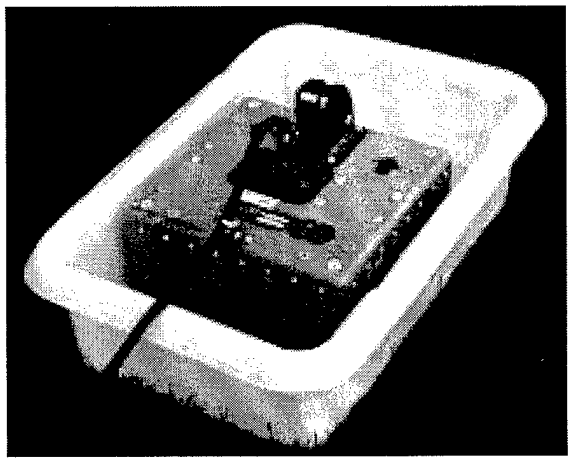

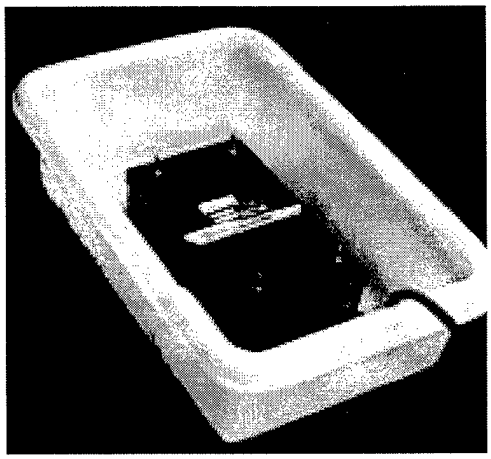

20000616 021

Approved for public release; distribution is unlimited.

DTIC QUALITY INSPECTED 4

Abstract: Ground-penetrating radar (GPR) was used to detect UXO and nonordnance on the 40-acre site (lot 54) of Jefferson Proving Ground, Indiana. The UXO are buried about 1 m deep in a clayey silt for which the soil water content ranged from moist near the surface to near saturation at about 1 m. A 16-bit radar was used to profile along previously established lines and transects over emplaced artificial targets. Data were recorded at 48–64 traces/s with minimal towing speeds during both dry and rainy weather. Target responses at both 300 (time range of 50 ns) and 600 MHz (30 ns) ranged from discrete diffractions to short reflection segments. Soil loss greatly attenuated diffraction hyperbolas. Theoretical analyses of these hyperbolas give an average soil dielectric constant of 10 at both 300 and 600 MHz. The phase polarity of many of the reflected and diffracted wavelets indicate targets with wave impedances higher than that of the soil. It is therefore assumed that these targets are metallic and the responses of some, whose locations correlate with the position of UXO on burial maps, are shown in detail. Theoretical modeling of wavelet propagation for this soil confirms the high rate of attenuation (47–66 dB/m round-trip), the maintenance of waveform, a shift in wavelet local frequency, and response to a typical UXO. It is concluded that GPR is effective for finding targets in this type of soil to no more than 2-m depth. It is recommended that future surveys utilize high trace acquisition rates to capture the full target responses, and a prowed, heavy dielectric antenna sled to improve antenna-to-ground coupling and to deflect surface obstacles such as vegetation. Broadband, three-dimensional numerical modeling of scattering from UXO-shaped targets in soil, with diverse orientations of antenna and target relative to one another, suggests that target length and diameter may be inferred from resonance patterns in backscattered signals. The simulations also reveal some ways in which oblique target/antenna orientations along a transect may affect frequency-dependent response patterns, providing clues as to target shape as well as positional ambiguities.

COVER: *Commercial antenna transducer units that produced the 300- (left) and 600-MHz wavelets. The plastic tubs improved ground contact.*

How to get copies of CRREL technical publications:

Department of Defense personnel and contractors may order reports through the Defense Technical Information Center:

DTIC-BR SUITE 0944
8725 JOHN J KINGMAN RD
FT BELVOIR VA 22060-6218
Telephone (800) 225-3842
E-mail help@dtic.mil
msorders@dtic.mil
WWW http://www.dtic.mil/

All others may order reports through the National Technical Information Service:

NTIS
5285 PORT ROYAL RD
SPRINGFIELD VA 22161
Telephone (703) 487-4650
(703) 487-4639 (TDD for the hearing-impaired)
E-mail orders@ntis.fedworld.gov
WWW http://www.ntis.gov/index.html

A complete list of all CRREL technical publications is available from

USACRREL (CEERD-IM-HL)
72 LYME RD
HANOVER NH 03755-1290
Telephone (603) 646-4338
E-mail erhoff@crrel.usace.army.mil

For information on all aspects of the Cold Regions Research and Engineering Laboratory, visit our World Wide Web site:

http://www.crrel.usace.army.mil

PREFACE

This report was prepared by Dr. Steven A. Arcone, Research Geophysicist, Snow and Ice Division; Dr. Kevin O'Neill, Research Civil Engineer, Applied Research Division; Allan J. Delaney, Physical Sciences Technician, Snow and Ice Division; and Paul V. Sellman, Geologist, Civil Engineering Research Division, Research and Engineering Directorate, U.S. Army Cold Regions Research and Engineering Laboratory (CRREL), Engineer Research and Development Center (ERDC), Hanover, New Hampshire.

This work was jointly sponsored by the U.S. Army Environmental Center (AEC), Aberdeen Proving Ground, Maryland, under MIPR Number 3767, 15 April 1997, George Robitaille, Program Manager, and by the ERDC Environmental Quality Technology (EQT) Program, Work Unit *Innovative Geophysical Technologies for Enhanced Buried UXO Discrimination* (AF25, 6.2), Dr. John Cullinane, Program Manager.

The authors thank Dr. Dwain Butler, Dr. Janet Simms, and Jose Llopis of Geotechnical Laboratory, ERDC, Vicksburg, Mississippi, for supplying necessary technical information and for helping to coordinate field activities, and thank the Thayer School of Engineering Numerical Methods Laboratory, particularly Dr. S.A. Haider, for providing technical assistance.

This publication reflects the personal views of the authors and does not suggest or reflect the policy, practices, programs, or doctrine of the U.S. Army or Government of the United States. The contents of this report are not to be used for advertising or promotional purposes. Citation of brand names does not constitute an official endorsement or approval of the use of such commercial products.

CONTENTS

Preface ii
Introduction 1
Site description 1
Soils 2
Dielectric theory 3
Equipment and methods 3
    Radar system 3
    Field profiling 4
    Post-processing and display of data 5
    Profile interpretation 5
Results and discussion 5
    Control studies 5
    Grid survey: 300 MHz 8
    Grid survey: 600 MHz 12
    Distribution of ε' 12
Theoretical discussion 13
Modeling 15
Incident field and polarization parameters 22
Modeling results 23
Conclusions and recommendations 28
Literature cited 30
Abstract 32

ILLUSTRATIONS

Figure

1. Location of the 40-acre site at Jefferson Proving Ground 2
2. Typical form of a radiated GPR wavelet 4
3. Distributions at the 40-acre site with radar profile transects superimposed 6
4. 300- and 600-MHz diffraction profiles and waveform responses to a metal disk buried 58 cm deep 7
5. Soil moisture profiles at five locations 7
6. Sample segment of a 300-MHz profile and the result of applying a background removal filter 10
7. Selected target responses within segments extracted from the 300-MHz profiles, and sample traces containing diffracted or reflected wavelets 10
8. Likely interpretations for two of the responses in Figure 7 13
9. Selected target responses within segments extracted from the 600-MHz profiles, and sample traces containing wavelets 14

10. Distribution of ε' at both 300 and 600 MHz 15
11. Dielectric permittivity curves and attenuation rates for the average ε', range of σ, and probable values of f_{rel} and ε_{oo} at JPG 16
12. Model 400-MHz wavelets before and after round-trip propagation within 1 m of ground characterized by the soil parameters measured 17
13. Radiation beamwidths for a model of our antennas and the average $\varepsilon' = 10.4$ found at JPG 21
14. Basic setup, with target below ground surface, in its reference orientation 23
15. Normalized scattered electric field above a projectile surrounded by soil and oriented in the Y direction, as a function of frequency 24
16. Normalized scattered E field above target for various projectile inclinations and rotations θ_d, θ_x 25
17. Normalized scattered E field when projectile axis is in (x,z) plane, from different vantage points Z_a, with different declinations θ_d 25
18. Backscattered E_z field magnitudes along transect, at various frequencies, when the projectile is inclined at 45° with nose up, and the antenna is rotated 26
19. Backscattered E_z field magnitudes along transect, at various frequencies, when the projectile is inclined at 45° with nose down, and the antenna is rotated 27
20. Scattered $|E_z|$ values, when the incidence direction and incident E field orientations are in the (x,z) plane, for various incidence angles 28

UXO Detection at Jefferson Proving Ground Using Ground-Penetrating Radar

STEVEN A. ARCONE, KEVIN O'NEILL, ALLAN J. DELANEY,
AND PAUL V. SELLMANN

INTRODUCTION

The remote detection of unexploded ordnance (UXO) has generally relied on the electromagnetic induction (EMI) and ground-penetrating radar (GPR) methods. EMI, the most common method, finds targets that contrast strongly in electrical conductivity with their host soil by detecting 10- to 40-kHz magnetic fields induced from the target. EMI systems are mobile and do not require ground contact, and their performance is not degraded by minor variations in topography. However, they have little ability to detect nonmetallic targets. GPR, which generally operates between about 50 and 1000 MHz, is sensitive to contrasts in both conductivity and dielectric permittivity. Thus GPR can detect plastic, glass, concrete, or wood when their permittivity contrasts with that of a moist soil. In addition, GPR shows the continuity of soil horizons and thus can detect burials of foreign targets by the disturbance of those horizons. GPR performance requires good antenna–ground contact and a complex soil permittivity and conductivity that does not rapidly attenuate radiowave energy. The 50- to 300-MHz range usually provides optimum penetration for a given soil conductivity and permittivity. In this report we discuss GPR results from a site within the Jefferson Proving Ground (JPG), where ordnance is buried within a highly attenuating soil and for which reports of GPR performance (NAVEOD 1997) are negative.

Our objectives were 1) to assess the ability of GPR to detect UXO-type targets at JPG, and 2) to understand the nature and causes of target responses to foster better target discrimination or explain difficulties therein. We were interested in the effect of the soil electrical properties upon the GPR survey parameters of frequency, towing speed, and data acquisition rate. We surveyed a site where the types, locations, depths, and approximate orientations of both ordnance (metallic) and nonordnance (metallic and nonmetallic) are documented. We used supplied location maps to identify the probable nature of targets detected. The specified depths are rarely stated to exceed one meter. We used a commercially available GPR system and towed 100-, 300- and 600-MHz- (mid-band values) frequency antennas along established lines. The higher two frequencies provide high resolution of subsurface objects and are within military specification for ordnance detection, and the antennas are small and mobile. We used the signal characteristics obtained from ordnance, nonordnance, and objects we emplaced to determine soil permittivity and diffraction waveforms.

Three-dimensional numerical modeling employed an integral method that allowed incorporation of a reasonably realistic subsurface antenna radiation pattern as well as arbitrary target shape and orientation. Key idealizations were the assumption of homogeneous ground and exclusion of ground surface effects. The model was used to compute fully polarimetric mono- and bistatic scattering over a broad band, for positions directly over a target as well as along a continuous transect passing by the target.

SITE DESCRIPTION

JPG (Fig. 1) is located in southern Indiana. Our investigations were performed within lot 54, known as the 40-acre site (Fig. 1). The vegetation at this site is

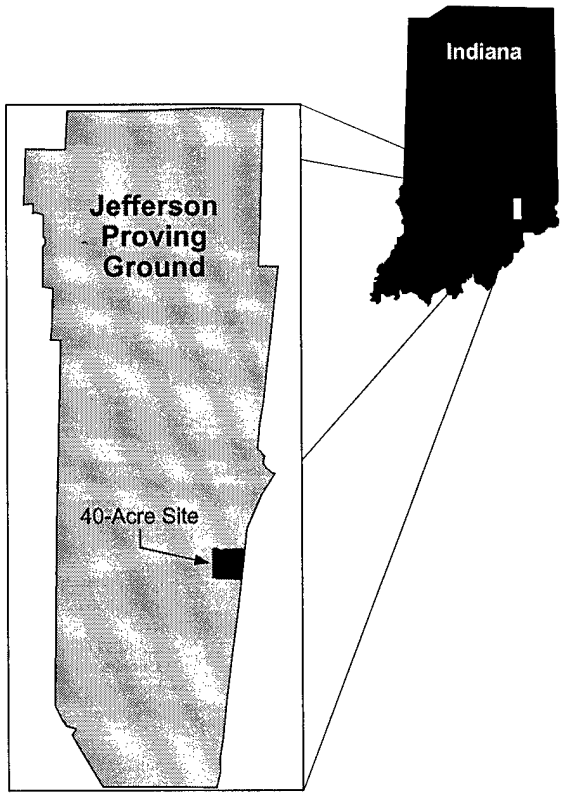

Figure 1. Location of the 40-acre site at Jefferson Proving Ground.

predominantly sedge and grass with a few trees. The area has a nearly level to gently sloping topography with small gullies providing only a few meters of relief. The site has been specially prepared with approximately 246 unfused, buried ordnance and 234 nonordnance targets buried within 1 m of the surface. The ordnance includes small, handheld munitions, 2-ft- (0.6-m-) long projectiles, and 5-ft- (1.6-m-) long bombs. Strong radio background noise was present at this site.

We conducted our surveys from 23 to 25 October 1997. The weather was clear on 23 October, and then light rain fell late on the 24th and all day on 25 October. All of our profile transects were freshly mowed, but clumps of woody vegetation and tractor ruts made for uneven antenna towing and short periods of poor antenna–ground contact.

SOILS

The soils in this area formed in a thin surface layer of windblown silt (loess) and underlying glacial drift (Nickell 1985). Some residual soils may reside near the limestone bedrock interface where small rock fragments occur. The bedrock ranges from about 1.5 to 7.6 m deep. The soils are part of either the Cobbsfork-Avonburg (CA) or Cincinnati-Rossmoyne-Hickory (CRH) soil map units. The CA soils are found on level to gently sloping surfaces, are generally poorly drained, and have a seasonally high water table. They can also have a pan layer, which can create a perched water table at a depth of 0.3–1 m for a significant part of the year. The CRH soils are found on level to steep surfaces and are classed as well drained to moderately well drained. They may also have a pan layer of low permeability and perched water tables at depths of 0.5–1 m during the winter and spring. In general, both soil units have a 15- to 20-cm surface soil consisting of silt loam varying from dark brown to gray brown. The permeability tends to decrease with depth because of an increase in clay content in the pan layers.

X-ray diffraction studies performed by the U.S. Army Waterways Experiment Station in Vicksburg, Mississippi, show the soil mineralogy to be primarily quartz and plagioclase feldspar with clay minerals generally absent or in minor amounts. This is consistent

with other studies of loess in the southern United States (Rodbell et al. 1997), which show a predominant amount of quartz, and also with studies of loess in interior Alaska (Péwé 1955).

DIELECTRIC THEORY

We present the theory of radiowave propagation in soils in this section in order to provide a basis for modeling the GPR propagation at JPG later. The discussion pertains to engineering-grade silt- and clay-size soils, but of little clay mineralogy so that it applies to the soils at JPG. The radar detectability of a subsurface target strongly depends on the radiowave speed, v, and attenuation rate, β, of the burial soil. The speed determines the shape of the antenna beamwidth. β determines how deep the radiowaves will penetrate and return to the surface with enough strength to be detected. These quantities are related to the relative complex permittivity of soil, ε_s^*, such that

$$v = c/\mathrm{Real}\,(\varepsilon_s^{*1/2}) \tag{1}$$

and

$$\beta(\mathrm{dB/m}) = 20\log\left(\exp\left\{i\omega/c\left[\mathrm{Imag}\left(\varepsilon_s^{*1/2}\right)\right]\right\}\right) \tag{2}$$

where $i = (-1)^{1/2}$, ω is frequency in radians/s, and $c = 3 \times 10^8$ m/s is the wavespeed in free space. The quantity ε_s^* is determined by the Debye relaxation permittivity (Debye 1929), ε_{rel}, and a contribution from the very-low-frequency soil conductivity, σ (Siemens/m, or S/m), such that

$$\varepsilon_s^* = \varepsilon_{rel} - i\sigma/\omega\varepsilon_0 \tag{3}$$

where

$$\varepsilon_{rel} = \varepsilon_{oo} + (\varepsilon_{st} - \varepsilon_{oo})/(1 + i\,f/f_{rel}). \tag{4}$$

ε_0 is the dielectric permittivity of free space (a constant), ε_{st} is the low-frequency, "static" value of the relative soil permittivity, ε_{oo} is the very-high-frequency value, $f = 2\pi\omega$ is the wave frequency in hertz (Hz), or frequency component for a radar wavelet, and f_{rel} is the soil relaxation frequency. The quantity ε_{rel} determines the dipole moment density induced in a material by a passing wave. The quantity f_{rel} is a characteristic frequency above which the induced dipoles no longer stay in phase with the incident radiowave. These dipoles then generate interference, which effectively slows and attenuates the incident radiation. This process is dispersive, which means that different frequencies within the incident wavelets propagate at different speeds and attenuation rates (Stratton 1941, Brillouin 1960, and Feynman et al. 1964).

Values of ε_{st} are directly related to the water content for nonmineralogic clays and silts (Topp et al. 1980) and generally equal ε_s^* for $f < 600$ MHz. Above about 600 MHz, laboratory investigations (Hoekstra and Doyle 1971, Hoekstra and Delaney 1974) show that the adsorbed water on the particle surfaces of the clay fraction (Tice et al. 1982) strongly influences the dielectric properties. The adsorption process lowers both the high dielectric constant (81) of the normally free water and also the free water relaxation frequency (22 GHz) to about 1–3 GHz. Values of ε_{oo} are generally related to the dry soil density, range from about 2.5 to 3.5, and equal ε_s^* at frequencies above about 100,000 MHz. For soils of JPG and the radar frequencies used, σ was large enough to also influence attenuation because it determines how much of the radiowave energy will be converted into conduction currents.

The resulting values of ε_s^* for silty and clay-rich soils at frequencies above about 100 MHz provide high values of β and wave speeds lower than would be expected for sandy soils with the same volumetric water content. The β values (a quantitative discussion is given later) increase as f approaches, and then exceeds, f_{rel}, and are orders of magnitude greater than attenuation rates caused by the geometric spreading of the radiation energy. At frequencies below about 1000 MHz, the real part, $\varepsilon' = \varepsilon_{st}$, often referred to as the dielectric constant, determines the wave speed v through the relation

$$v = c/\varepsilon'^{1/2} \tag{5}$$

for a variety of frozen and unfrozen silts and (nonmineralogic) clays (Hoekstra and Delaney 1974, Topp et al. 1980, Delaney and Arcone 1984).

EQUIPMENT AND METHODS

Radar system

We used the GSSI (Geophysical Survey Systems, Inc.) SIR system model 2 and models 3207 (100 MHz), 5103 (300 MHz), and 101C (600 MHz) antenna transducers. We used the control unit to set the time range (in nanoseconds, ns) for the echo traces, the data acquisition rate (48 or 64 traces/s), the sampling density (512 samples per trace), trace sample density (16-bit), and time variable gain (TVG) for the traces. We calibrated our settings with the antennas set over targets

that we emplaced. The resulting reflections required a large amount of gain (up to 65 dB) at time ranges of only 50 (300 MHz) and 30 ns (600 MHz). The short time ranges were sufficient to capture target responses throughout the site but were also necessary to limit background radiowave interference, which beat with the radar returns at the high-gain time ranges. The high gain had the negative effect of amplifying small antenna impedance mismatches and low-amplitude clutter (unwanted events), which probably originated from radiation that leaked onto the antenna housing and cables. These events usually arrive at constant time delay and their interference can be alleviated with a horizontal "background removal" filter. However, in our case, where short time ranges were used, electronic jitter and erratic movement of the antenna may have caused these events to arrive at variable amplitude and so their interference was not consistently reduced by filtering.

All antennas were resistively loaded dipoles. The smaller, 300- and 600-MHz antennas are shielded with semi-cylindrical housings to alleviate above-surface clutter. These frequencies are "local" (also known as "instantaneous") values, which correspond with the dominant periods and lie approximately at the center of the received wavelet spectrum. They are considerably below the manufacturer's specifications for these antennas (400 and 900 MHz, respectively), which generally apply to operation in air or on the ground with lower values of dielectric permittivity and loss than encountered here. Their transmitters do not exceed 8 W (peak power) in order to protect the nearby receiver. One-hundred-MHz data were also acquired but are not discussed because the direct coupling between these antennas, which lasts approximately 30–50 ns, obliterated any near-surface returns. The antenna directivity becomes increasingly confined beneath the antenna as ε' increases (Arcone 1995). The typical shape of a transmitted GPR wavelet for either the 300- or 600-MHz antenna system is shown in Figure 2. The phase polarity sequence of the half-cycles defines the wavelet phase (Arcone 1995).

Field profiling

We profiled along established transects and entered electronic event markers on the profiles at previously established, 100-ft (30-m) distance marks. The transects generally deviated from a straight line by 1–2 m, and sometimes by as much as 5 m to avoid isolated bushes, trees, and severe ruts. Consequently we cannot reconstruct our exact position along the lines, and errors of as much as 20 ft (6 m) may occur in our interpretation of distance between markers. We dragged all our antennas by vehicle at less than 1 m/s for long distances and by hand for the small surveys over emplaced targets. All antennas were polarized perpendicular to the transect direction. We determined that vehicle reflections were not in the data by comparing profiles recorded with and without the vehicle. We placed the smaller antennas in a fiberglass box to alleviate erratic antenna-to-ground coupling. However, the uneven towing speed over the rough ground also degraded the appearance of the profiles.

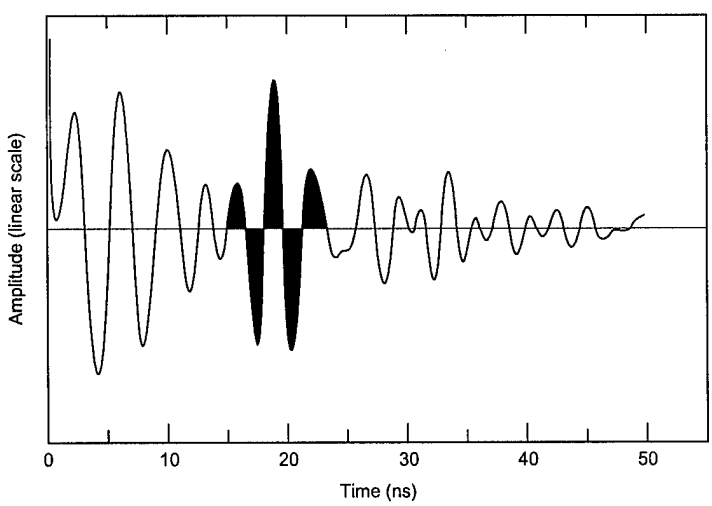

Figure 2. Typical form of a radiated GPR wavelet (darkened area). The frequency characterization of the wavelet refers to the inverse of the dominant wavelet period (in this case, about 300 MHz).

Post-processing and display of data

We first band-pass-filtered (very wide settings, e.g., 50–600 MHz for the Model 5103 antenna) the recorded data to alleviate high-frequency electronic noise and low-frequency, above-surface clutter. We normalized the number of data traces between event markers over the targets we emplaced to compensate for changes in dragging speed. We did not normalize the longer profiles with the 100-ft (30-m) marker spacing because vehicle speed varied between any two markers.

We used both linear and nonlinear gray-scale formats to indicate signal strength, and used an amplitude format to display the profiles for the targets we buried. In this format, positive phase is indicated by lighter tones and negative phase by darker tones. We used an intensity format to display the profiles of the permanent targets at JPG. In this format, which is insensitive to phase, strength is indicated by the intensity of darker tones.

Profile interpretation

The main objectives of the profile analysis are to determine if ordnance targets had been detected and the range of ε'values for the site soil. The permittivity analysis used the diffractions caused by radar scattering from targets. In this method we matched the hyperbolic shape of the diffractions with theoretical hyperbolas for a given value of ε' (Jezek et al. 1979, Clarke and Bentley 1994, Arcone et al. 1998). The main disadvantages of this approach are 1) the hyperbolas can actually be responses to linear soil inclusions, in which case the hyperbolas are distorted reflections that result when the transect obliquely intersects the inclusion direction (Jezek et al. 1979) and are thus artificially wide; and 2) an erratic towing speed, which would distort the hyperbolic image. Item 1 was not considered important because of the depositional process of the soil (glacial drift and loess) and because of probable historical tilling. Item 2 is a concern and for this reason a statistical study is presented.

Target detection depends on the presence of either or both diffractions and reflections and also on their phase polarity. Both the strength and phase polarity of a reflected or diffracted event depend on the reflectivity of a target, which is determined by its Fresnel reflection coefficient, R, such that

$$R = (\varepsilon_s{}^{*1/2} - \varepsilon_t{}^{*1/2})/(\varepsilon_s{}^{*1/2} + \varepsilon_t{}^{*1/2}) \qquad (6)$$

where $\varepsilon_t{}^*$ is the complex permittivity for the target medium (Wait 1970). Although this formula applies to plane wave incidence upon large flat reflectors, we invoke its use because of the small in-situ wavelengths (30 cm at 300 MHz) relative to the larger sizes of some of the targets known to be buried at JPG and because it predicts the correct phase polarity. For a metal target, assumed to be ordnance, $\varepsilon_t{}^*$ is orders of magnitude higher than $\varepsilon_s{}^*$ and produces a wavelet with a phase structure opposite to that produced when $\varepsilon_t{}^*$ is lower than $\varepsilon_s{}^*$.

It is unlikely that any geologic or organic inhomogeneity in the JPG soil we profiled had a higher $\varepsilon_t{}^*$ than that of the soil itself. Consistent horizons are virtually absent in our data, which means that electrically important changes, such as in moisture content, were gradational. In addition, $\varepsilon'$of limestone is generally between 8 and 10 (Parkhomenko 1967), which is near that of the soil and precluded strong bedrock reflections.

RESULTS AND DISCUSSION

Control studies

Our objectives for the control studies were to obtain profile responses and scattered waveforms for buried metal reflectors, as well as soil moisture and conductivity profiles. We conducted these studies either outside or along the perimeter of the 40-acre site (Fig. 3). We buried two 9-inch- (23-cm-) diameter metal disks at depths of 11 (28 cm) and 23 (58 cm) inches. The removed soil was highly compact and did not appear to have excess moisture. Therefore, we think that no significant soil drying took place between removal and reburial. The 300- and 600-MHz diffractions from the deeper target (Fig. 4) (the response to the more shallow target is not sufficiently separated from the direct coupling between antennas to facilitate analysis) best fit theoretical diffraction hyperbolas for $\varepsilon' = 9.3$ and 8.6 at 300 and 600 MHz, respectively. The values of ε', which we computed from the wavelet round-trip travel time when the antennas were over the center of the targets, are 9.5 and 8.7, respectively. In accordance with the measurements, dielectric dispersion theory (eq. 4, and discussed below) predicts that the 600-MHz value should be slightly less than the 300-MHz value.

The accompanying traces in Figure 4, whose positions within the profiles are indicated by arrows, show the forms of the scattered wavelets within the diffractions. The wavelets have a negative–positive–negative sequence to the phase polarity of the dominant half-cycles. This sequence is typical for the relative polarity wiring of these GSSI antennas and is characteristic of targets whose wave impedance (eq. 6) is higher than that of the surrounding media. Targets characterized by an ε' value less than that of the soil matrix would produce a similar wavelet but with opposite phase polarity of the individual half-cycles. The local frequency is indicated for the wavelets.

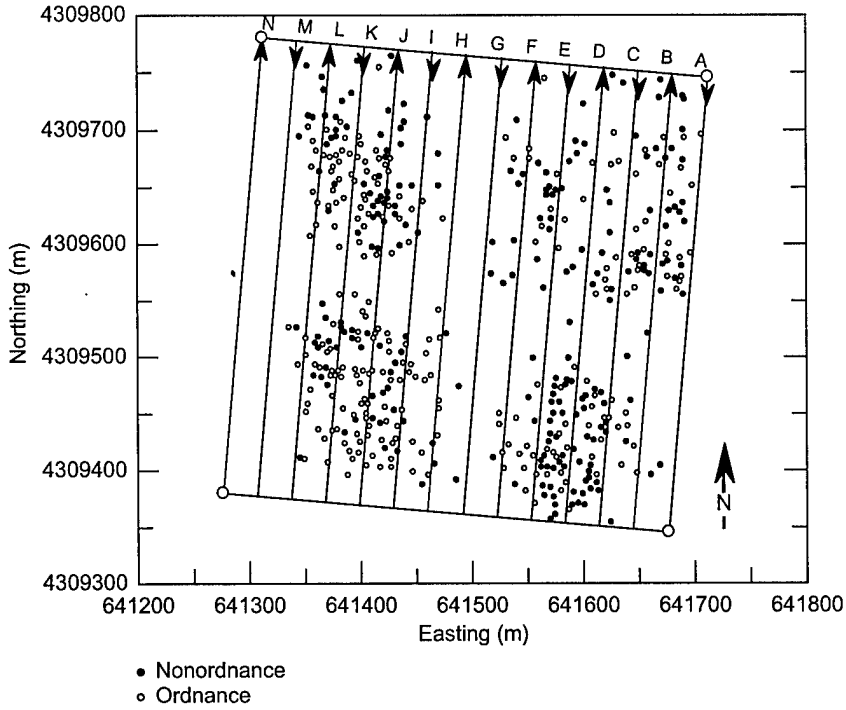

a. Ordnance and nonordnance distributions.

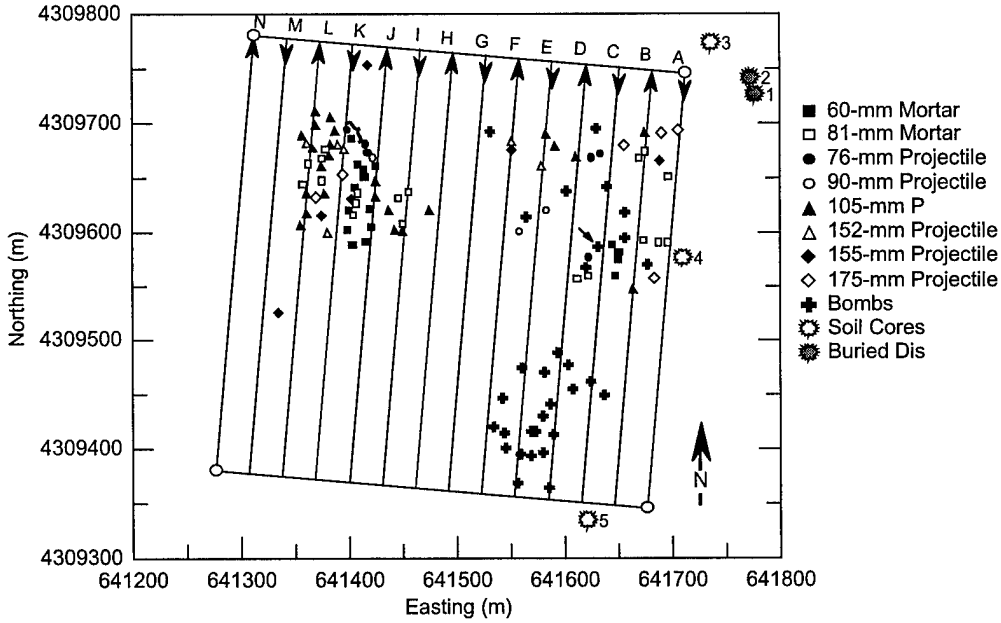

b. Ordnance-type distributions.

Figure 3. Distributions at the 40-acre site with radar profile transects superimposed. Line arrows indicate the profile directions. In Figure 3b, the small arrow along line C marks a bomb (cross symbol), and a bracket along line K indicates targets whose responses are discussed later. Also shown are the locations of the targets we buried and the soil cores we extracted for moisture profiles.

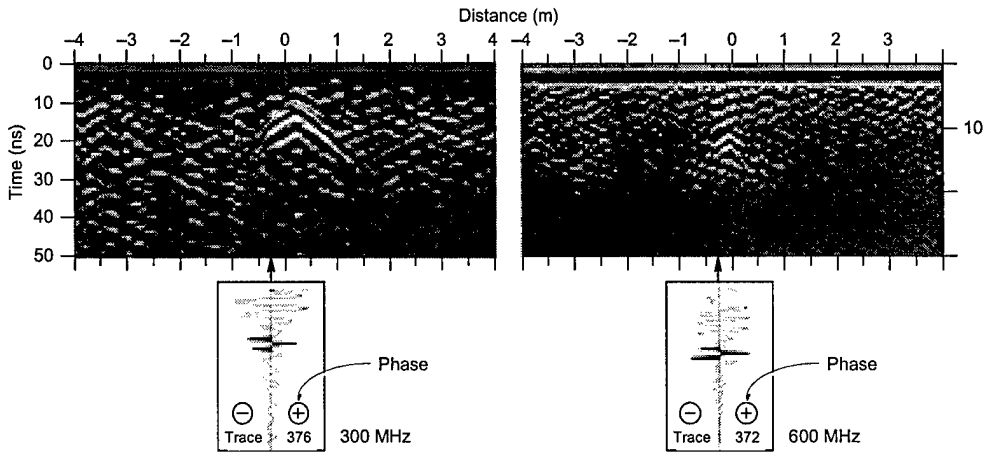

Figure 4. 300- (left) and 600- (right) MHz diffraction profiles and waveform responses to a metal disk buried 58 cm deep. The amplitude of the 600-MHz diffraction fades rapidly as distance increases from the target. The diffracted wavelets (darkened areas) within the sample traces have a half-cycle polarity sequence that is characteristic of the response of this antenna system's wavelets from a metal target.

The amplitude along the 600-MHz hyperbolic asymptotes in Figure 4 rapidly fades with distance from the target. This indicates a very high soil attenuation rate per meter; the change in antenna directivity with angle to the target (discussed later) is an insignificant loss factor. Commercial GPR systems at these frequencies commonly have a performance figure of about 100–120 dB and a dynamic range (the amplitude range visible in any particular trace) of about 60–70 dB. This latter range is consistent with the gain we added before recording and with soil attenuation rates discussed later.

The volumetric water content profiles of soil core samples (obtained before rain occurred) show values from about 15% at the surface to as high as 40% at 30–180 cm deep (Fig. 5). The water contents within the profile of the core obtained about 24 hours after steady rain had begun ranged from 23 to 45%, the latter of which is at about saturation for this type of soil. The

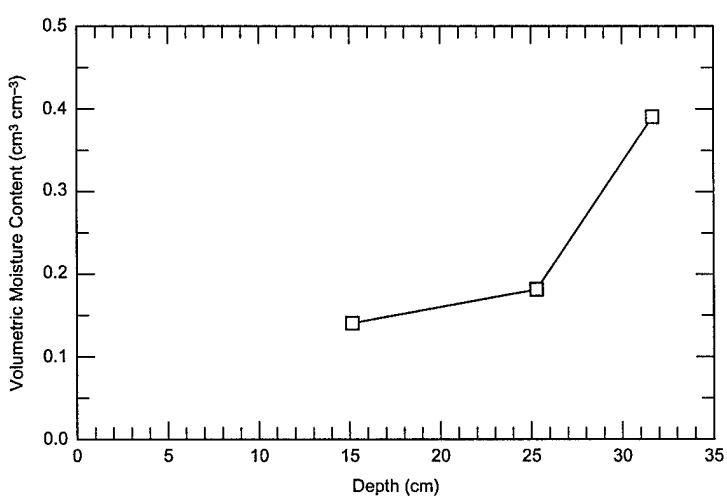

a. Profile 1.

Figure 5. Soil moisture profiles at five locations.

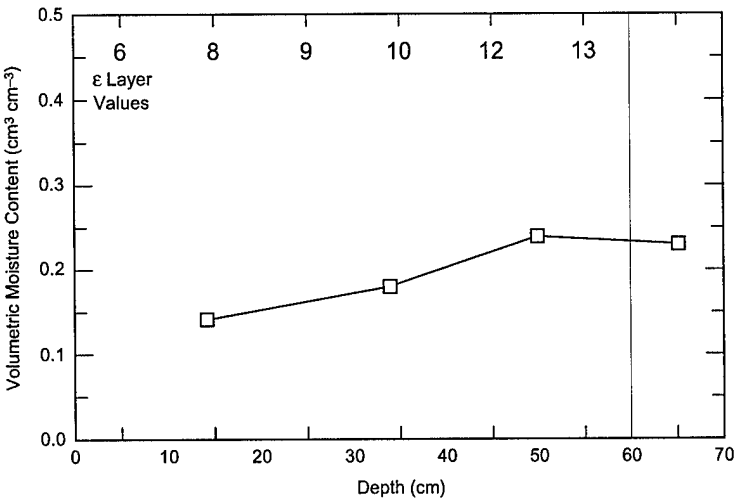

b. Profile 2.

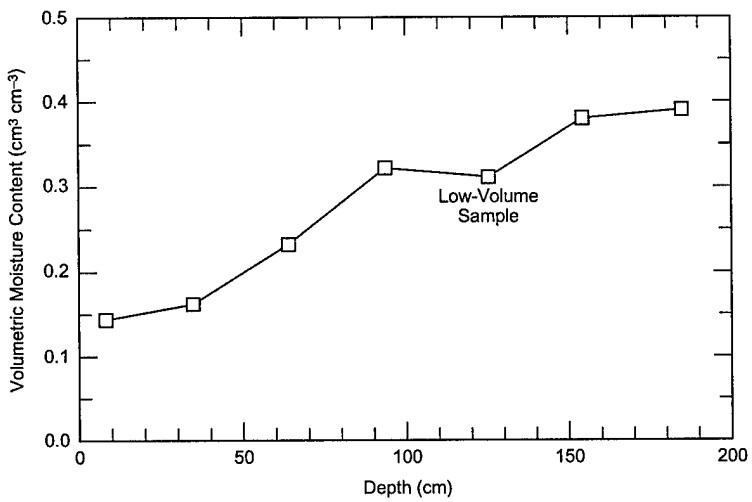

c. Profile 3.

Figure 5 (cont'd). Soil moisture profiles at five locations.

core obtained above the 58-cm-deep target showed a moisture content that varied from 15% at 15 cm deep to 24% at 50–70 cm deep. According to Topp et al. (1980), these water contents correspond with ε' values ranging from about 7 (15%) to 12 (25%), which agrees well with our values of 8.6–9.5 for this soil column. A time-of-flight analysis, in which we ascribed the appropriate ε' to 10-cm soil increments (Fig. 5b) and then calculated the time delay in each increment, gives an effective ε' value of 9.5.

Soil conductivity, σ, was measured at several sites by the Waterways Experiment Station (Llopis in prep). Using four-electrode Schlumberger soundings, concurrent with our work, they found the soil resistivity structure to be dominated by a near-surface, 2- to 4-m layer with approximately $0.025 < \sigma < 0.04$ s/m. These values strongly influence radiowave attenuation below about 400 MHz, while the imaginary part of ε^*, ε'', influences attenuation above 400 MHz (discussed later). Although ε'' was not measured, the high amount of gain used for the radar measurements indicates a high attenuation rate for this soil and will be seen to be consistent with the above range of σ.

Grid survey: 300 MHz

The transect lines on the 40-acre site are superimposed on maps of target and ordnance distribution in Figure 3. The lines surveyed are designated as transects A, B, C, etc., and were 1300 ft (396 m) long. The class of target (ordnance or nonordnance) is indicated on the map. Additional information regarding exact location and type of target, target depth, and approximate orientation is available. All ordnance are metal.

We show a typical 300-MHz profile segment before and after horizontal background removal filtering in Figure 6. Intensity is linearly proportional to signal ampli-

d. Profile 4.

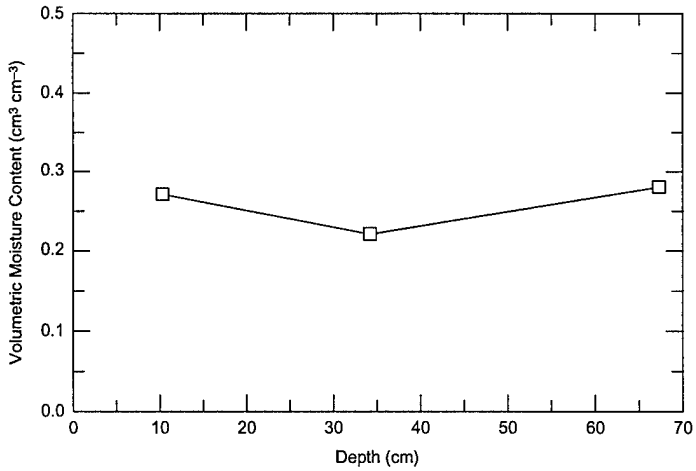

e. Profile 5.

Figure 5 (cont'd).

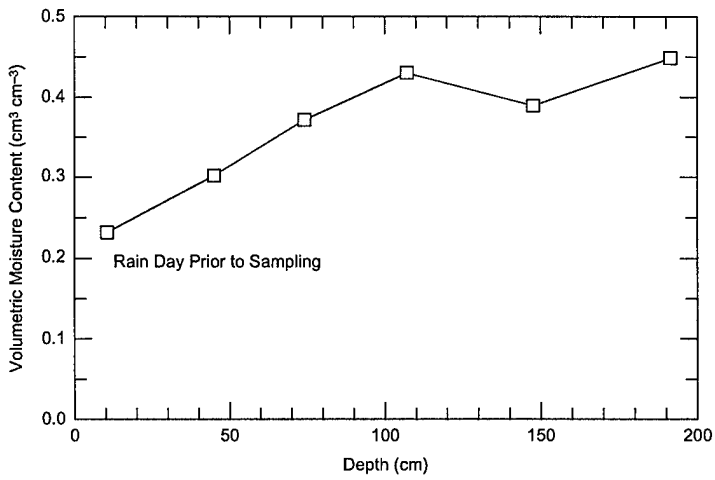

tude in the profile. The time range of 50 ns, beyond which noise became severe, corresponds to about 2.3 m of penetration for $\varepsilon' = 10.4$, the average value obtained at JPG (discussed later). The direct coupling between antennas occupies about 8 ns of the record and masks part of the responses to some of the targets. The noise bands between about 30 and 40 ns are probably caused by radiation leakage onto the cables that reflected back to the receiver and internal system mismatch reflections caused by either the high value of ε' at the surface or poor system design. In both cases, erratic ground contact, caused by uneven topography and jerks in the towing, caused the amplitude of these bands to vary and precluded the efficacy of horizontal filtering. No distinct and extended horizons indicative of soil stratification or a bedrock interface appear within the 2–3 m of radar penetration along any of our profiles.

We use arrows to identify several targets of anomalously high amplitude in the unfiltered profile of Figure 6. These targets are characterized by both hyperbolic diffractions (between 859 and 865 ft) and short reflection segments. Although the background filtering reduces the noise bands and the direct coupling, it also attenuates many target responses, especially those characterized by short reflection segments such as occur near 926, 915, and 900 ft. The use of more traces (i.e., a wider "window") in the background filter would retain these reflection responses at the expense of less noise reduction.

In general, we detected a total of 30 high-amplitude targets along all 14 lines, of which 14 responses within segments of these profiles are shown in Figure 7. The phase structure of several of the target wavelets (transects C, left; G, left; K, left; and I) identifies them as being of higher impedance than the surrounding soil matrix. They are therefore probably metal. Other target wavelets have a phase structure opposite that of the metal response (transect F; transect K, right). We presume these responses to be from the nonordnance targets. Some targets exhibit waveform resonance,

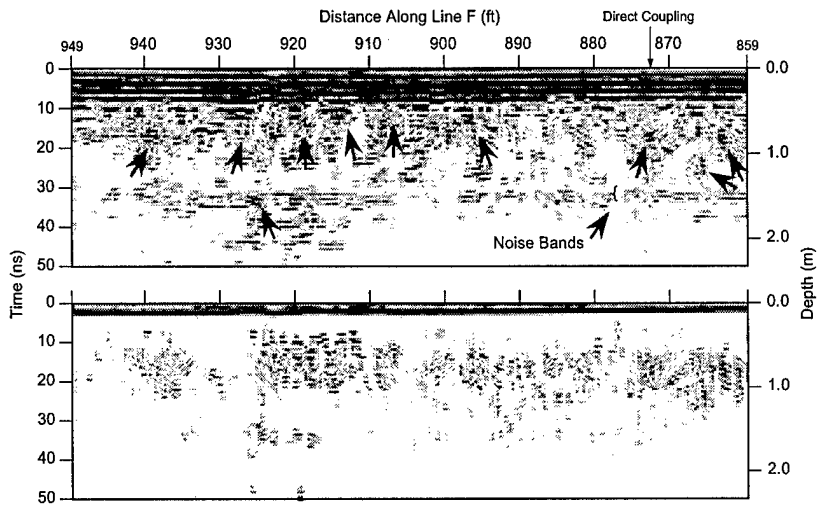

Figure 6. Sample segment of a 300-MHz profile (top) and the result of applying a background removal filter (bottom). The arrows indicate strong targets. The short filter window required to alleviate the erratic character of the background noise decreases the prominence of the target responses.

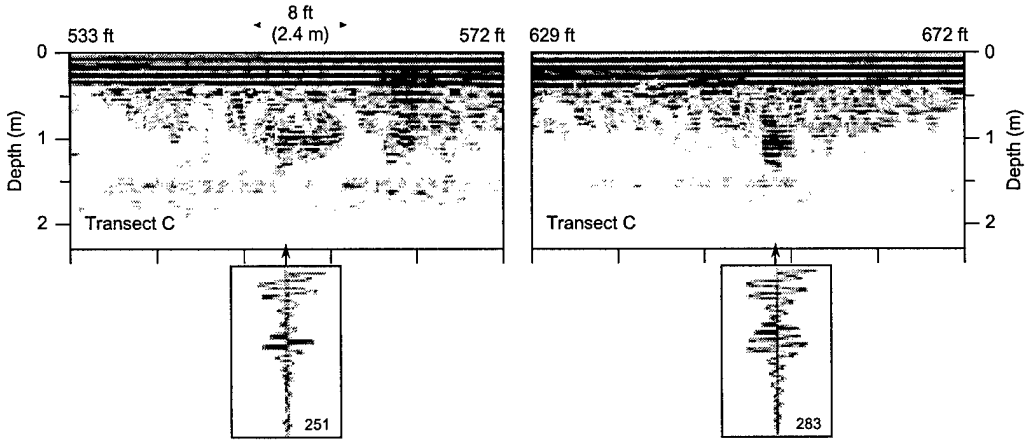

a. Transect C.

Figure 7. Selected target responses within segments extracted from the 300-MHz profiles, and sample traces containing diffracted or reflected wavelets (darkened areas). The distances along each transect are shown at the top of the segments. Each segment is 500 traces long, and trace number is indicated on the sample traces. The lower horizontal scale is in 100-trace increments. The depth scale is based on an ε' of 10.4.

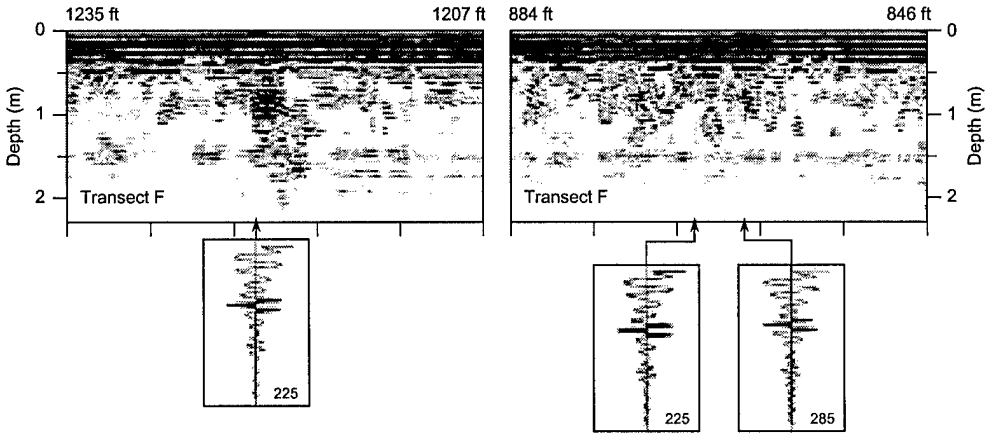

b. Transect F.

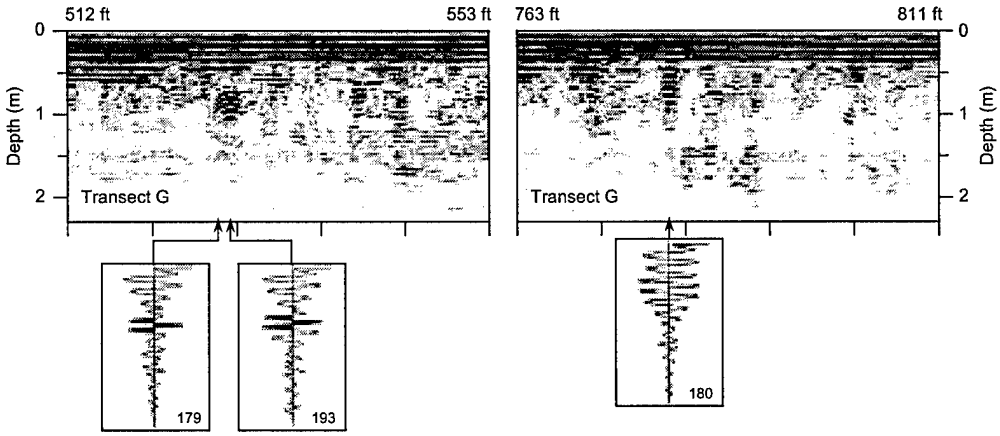

c. Transect G.

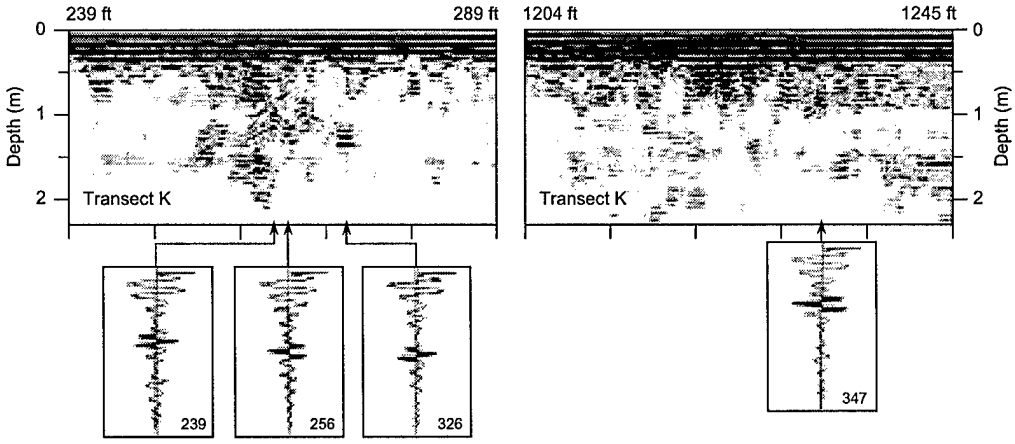

d. Transect K.

Figure 7 (cont'd).

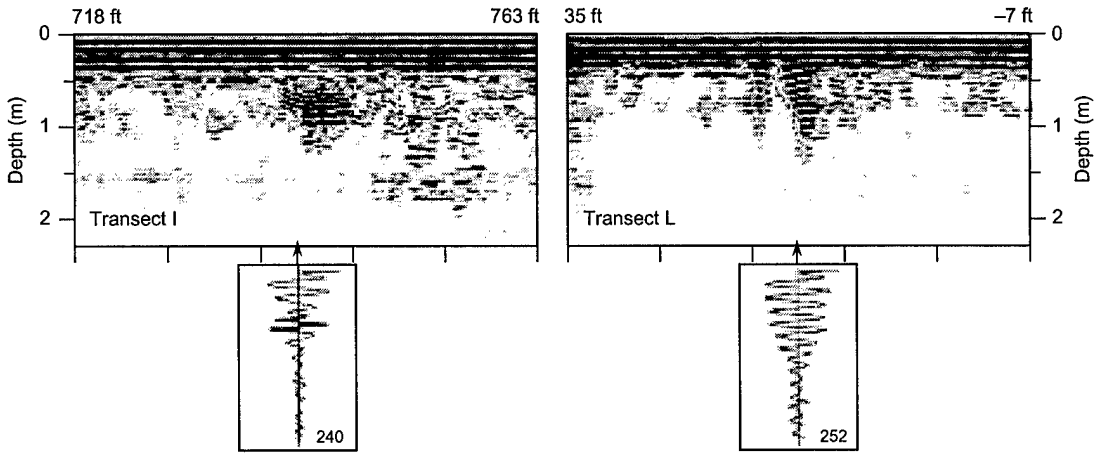

e. Transects I and L.

Figure 7 (cont'd). Selected target responses within segments extracted from the 300-MHz profiles and sample traces containing diffracted or reflected wavelets (darkened areas). The distances along each transect are shown at the top of the segments. Each segment is 500 traces long, and trace number is indicated on the sample traces. The lower horizontal scale is in 100-trace increments. The depth scale is based on an ε′ of 10.4.

within which the first few half-cycles have the metal response waveform (transect C, right), while other targets exhibit resonances within the direct coupling and cannot be similarly analyzed (transect G, right; transect L). These latter resonances occur where targets are extremely close to the surface; i.e., where target multiple reflections occur before soil attenuation dampens them significantly. In all cases, diffraction asymptotes are so highly attenuated as to be either barely visible for small targets (transect G, left), as was seen in the control studies of Figure 4, or not visible at all where they should occur at the ends of short reflection segments recorded above more extended targets (transect C, left).

We give probable interpretations for the target responses seen along transect C (left side) and along transect K (left side) in Figure 8. The response along transect C is about 7 ft (2.1 m) long, which is close to the length of a heavy bomb (1.6 m). The location of this response (533–572 ft) is marked in Figure 3b as having such ordnance. The more complex response along transect K is about 12 ft (3.7 m) long and occurs in a section marked as having several medium-size mortars and projectiles. The JPG UXO ordnance brochures show many of these projectiles to be about 2 ft (0.6 m) long. We therefore speculate that this transect segment spanned a series of close projectiles.

Grid survey: 600 MHz

We conducted this survey along four of the 14 grid lines. We show profile segments containing the seven strongest target responses (Fig. 9) in a nonlinear format because the amplitudes of all the returns are extremely weak, hence the appearance of much more noise (gray speckle patterns) in the profiles than appeared at 300 MHz.

Small segments of diffractions are apparent in all the target responses in Figure 9; the lack of asymptotes indicates the high signal attenuation. Almost all of the responses have well-defined wavelets that exhibit the proper phase for a high-impedance target. These responses originate from depths less than about 0.5 m and would not have been resolved from the direct coupling of the 300-MHz system. Although the time range is only 30 ns, very few target responses occurred at greater than about 20-ns range. Therefore, the penetration of this frequency in this soil was limited to less than 1 m deep.

Distribution of ε′

We compared the more prominent diffractions seen in both the 300- and 600-MHz surveys with model hyperbolas to produce distributions of ε′ and to compute an effective mean permittivity value for the over-

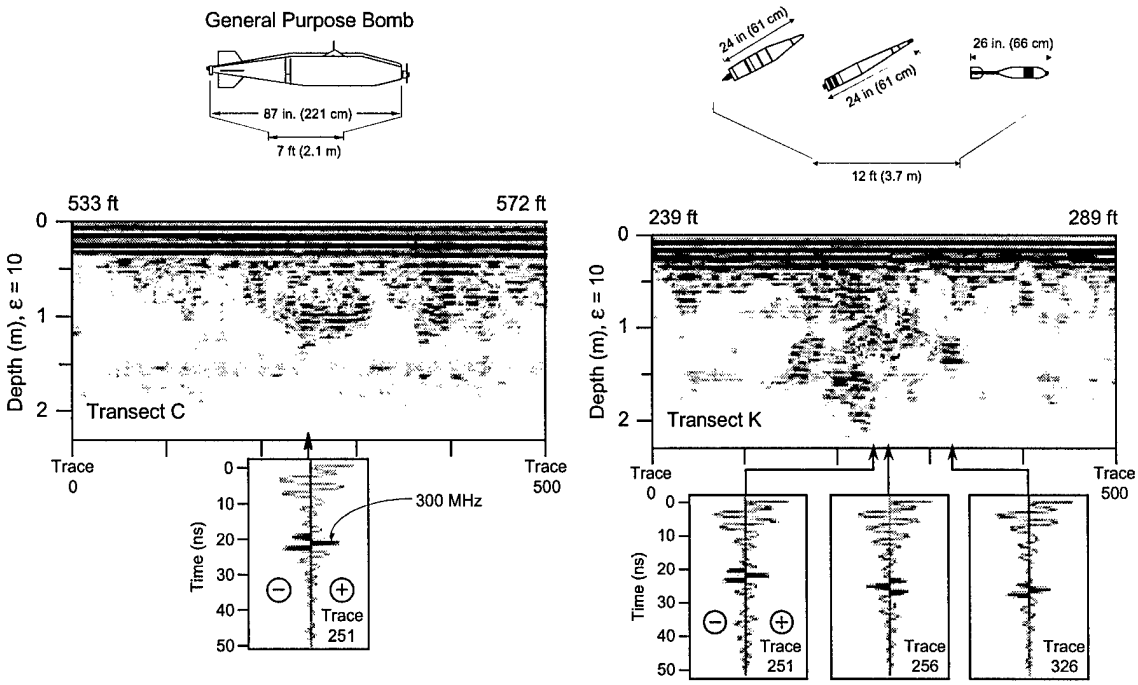

Figure 8. Likely interpretations for two of the responses in Figure 7.

burden above the targets. Seventy diffractions were identified in the 300-MHz survey and 48 in the 600-MHz survey. We used a statistical approach to average the computational inaccuracies caused by the minor differences in distance scale that resulted from uneven towing speeds. Seventy hyperbolas were clear enough in the 300-MHz profiles to be used and 48 in the 600-MHz profiles. Both distributions (Fig. 10) exhibit nearly the same average value and similar standard deviations (s.d.), although their distributions are slightly different. The 300-MHz distribution is more bimodal, which may reflect different orientations of deeper targets; extended targets whose axial direction crosses that of the transect produce hyperbolic reflections rather than diffractions, with values of ε' reduced by the sine of the intersection angle (Jezek et al. 1979). The 600-MHz distribution may reflect less target orientation because it was limited to only lines A–D and to shallower depths.

THEORETICAL DISCUSSION

The average values of ε', the range of σ, the fact that ε' may be slightly less at 600 MHz than at 300, and the high radar gain and faded diffraction asymptotes, both of which indicate high attenuation rates, allow us to estimate the soil dielectric properties at JPG (Fig. 11a) and theorize their effect upon antenna beamwidth and waveform. We assume f_{rel} is about 3 GHz (Hoekstra and Delaney 1974); if it was any lower, then ε' at 600 MHz would be distinctly lower than it is at 300 MHz. We chose a value of 3 for ε_{oo}, which is characteristic of dry soils and applies to frequency values where water is nondispersive. The JPG values of σ strongly influence β below about 400 MHz, while ε_{rel} is the dominant factor above about 400 MHz (Fig. 11b). Unfrozen mineralogic clays can exhibit even stronger absorption and may preclude any radar penetration at our frequency range and above (Hoekstra and Doyle 1971).

We computed the effects of the soil properties upon the round-trip propagation of both a model of our 300-MHz wavelet and an ideal monocycle-type waveform (Fig. 12). A monocycle is the shortest possible pulse an antenna can radiate and may be nearly achieved with unshielded antennas. It therefore has a wider bandwidth than our system model and would provide the highest possible target resolution. Both wavelets begin propagation with a local frequency of 400 MHz (Fig. 12a), which is that of our antenna model 5103 when used on

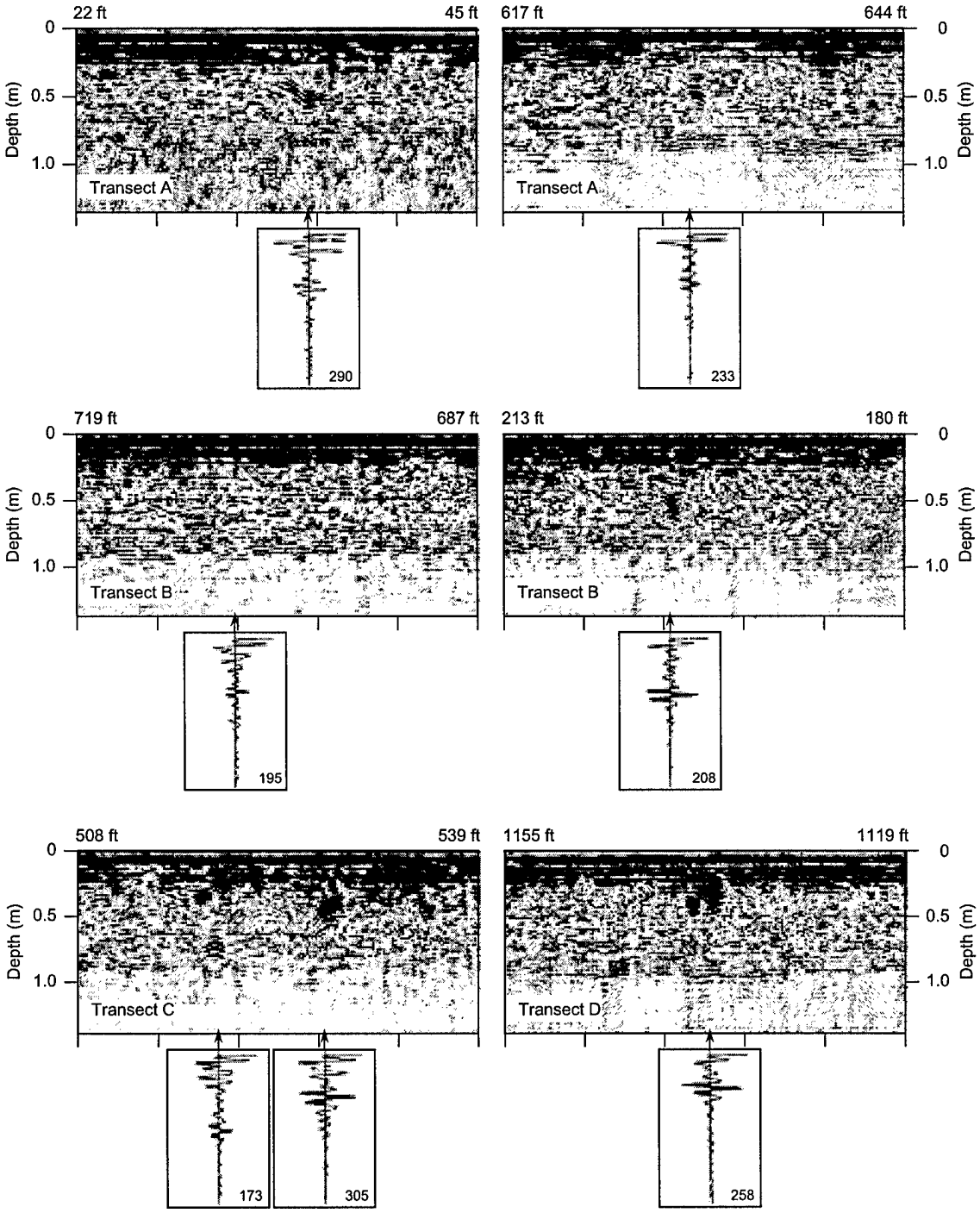

Figure 9. Selected target responses within segments extracted from the 600-MHz profiles, and sample traces containing wavelets. The penetration of this frequency is about 1 m.

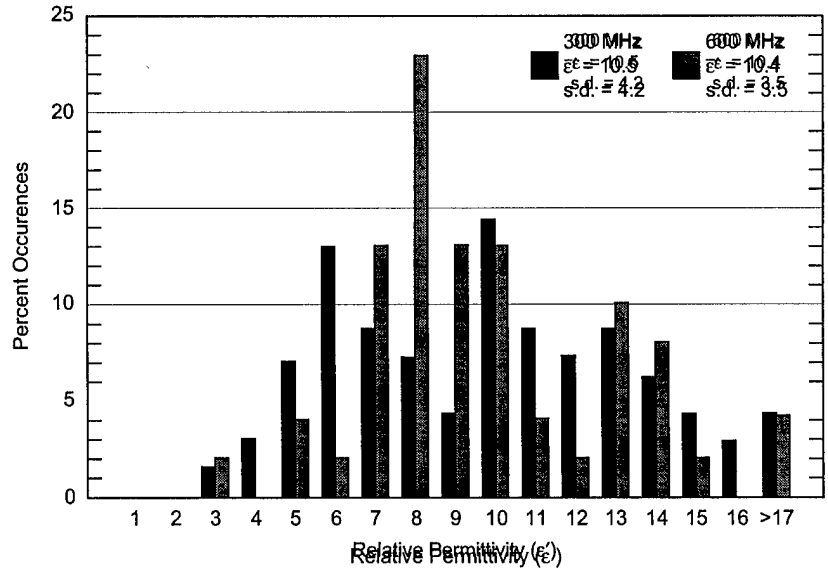

Figure 10. Distribution of ε′ at both 300 (black) and 600 MHz (grey).

low-permittivity material (e.g., $\varepsilon' = 4$). Both wavelets then experience strong attenuation caused by conductivity alone (Fig. 12b) but maintain their original form in this case and show no shift in local frequency*. Figures 12c and d show that shifts in local frequency will occur when the dielectric relaxation is considered. Despite the shift, the wavelet form is changed little.

The value of ε′ also determines the antenna directivity (Arcone 1995). Horizontal dipoles on the ground surface show a greater concentration of energy within the subsurface vertical plane that includes the antenna axis than in the plane perpendicular to the axis (Fig. 13). As ε′ increases, the radiation will become more confined within the plane containing the antenna axis. This means that our profiles were mainly sensitive to the ground directly beneath the transects. The greater width of the pattern perpendicular to the axis (and along our transects) shows that the rapid fading we observed within diffraction asymptotes was due to soil attenuation and not to radiation directivity.

*The distortion is small in all cases for our system model (Fig. 12b, c, d, bottom) and the attenuation is comparable to the gain we used during recording to bring reflections to the level of the direct coupling. The shift in local frequency for the ideal wavelet (Fig. 12c, d, top) is severe enough to preclude its detection by a receiver antenna identical to the transmitter antenna. In contrast, the local frequency of our system model is lowered to only 300 MHz by the 3-GHz relaxation frequency (Fig. 12c, bottom). A value of 6 GHz has less effect (Fig. 12d, bottom).

MODELING

In this section we describe some basic modeling that is intended to do two things: 1) demonstrate how the specific kinds of scattering effects from elongated UXO-type targets can give systematic clues to the character of the target; and 2) show how such scattering can cause ambiguities in the pattern of measured signal. As an entrance into modeling the kind of phenomena confronted in the field, we constructed a simple integral equation model of radar scattering in a uniform loessy background. Our focus is on the kinds of fields radiated from a dipole-type antenna, their interactions with UXO-form targets, and the scattered signals that result. We do not include complications here which may arise from the presence of a ground surface near the target, but concentrate only on the transmissions and reflections back and forth between the antenna and target. Elsewhere, using more sophisticated modeling techniques (O'Neill et al. in prep), we treat targets with proximate ground surfaces. These latter investigations generally reveal that basic resonance and polarimetric scattering phenomena that we see here using the integral equation model (infinite homogeneous soil background) usually persist when the target is near the ground surface.

Within the bounds of our assumptions–infinite soil constituting a uniform background around the target–we treat the physics of the antenna radiation and target scattering (re-radiation) rigorously. All governing relations used here begin with statements tantamount to Huygen's Principle (Kong 1990). To simulate both radiation from the buried target and from the transmit-

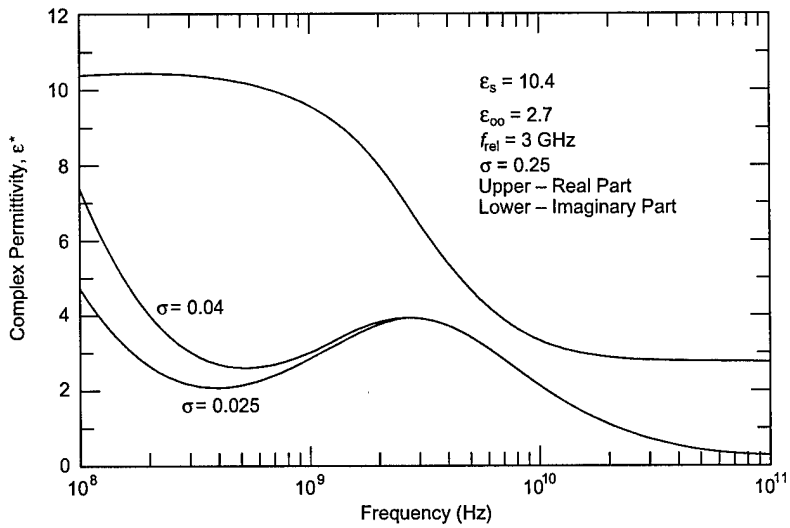

a. Dielectric permittivity curves.

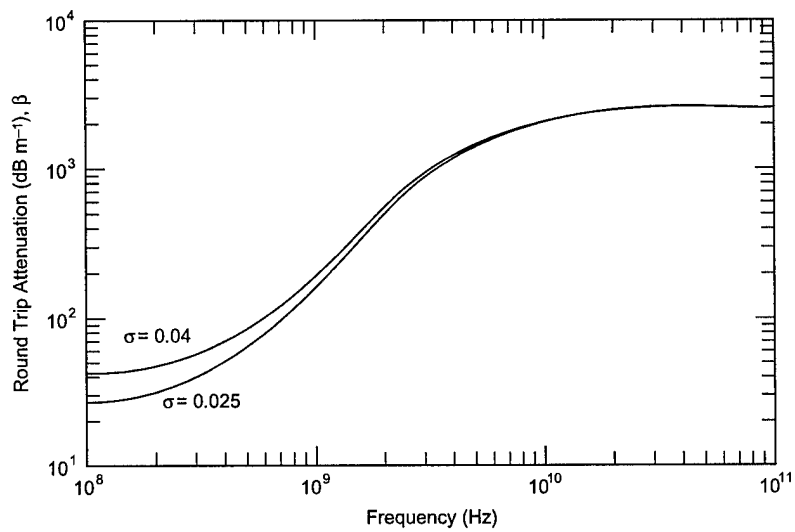

b. Attenuation rates.

Figure 11. Dielectric permittivity curves and attenuation rates for the average ε′, range of σ, and probable values of f_{rel} and ε_{oo} at JPG. A dielectric relaxation at about 3 GHz strongly increases β above about 300 MHz, yet wave velocity (determined by the real part of ε_s*) remains constant to about 600 MHz.

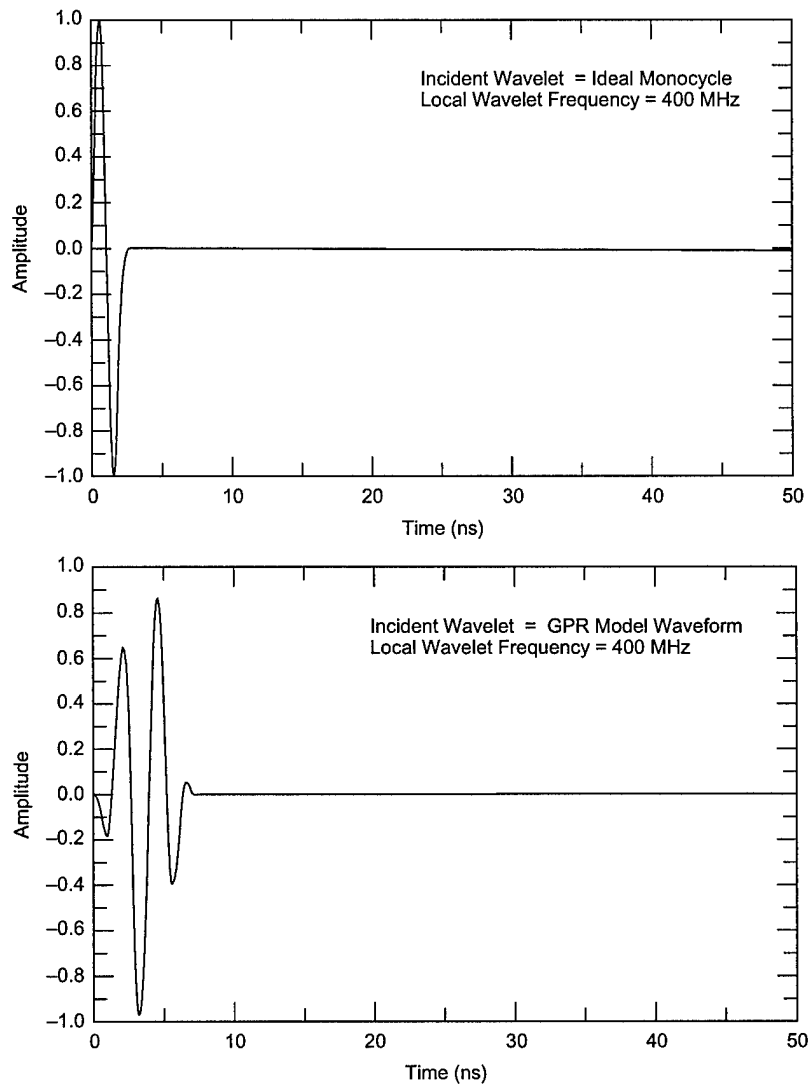

a. Incident waveforms.

Figure 12. Model 400-MHz wavelets before and after round-trip propagation within 1 m of ground characterized by the soil parameters measured. The wavelets reflect from an interface for which R = –1 (eq. 6), which only reverses the phase of the wavelets so that all wavelet distortion and attenuation are due to propagation.

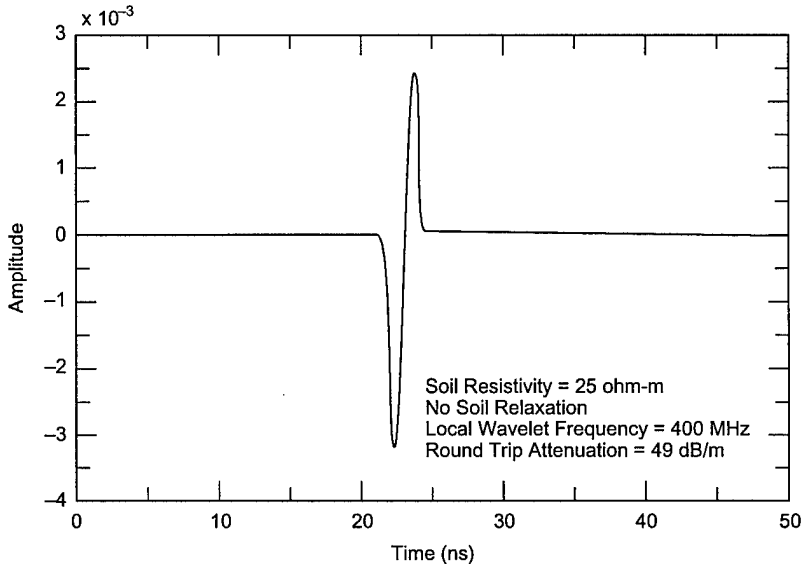

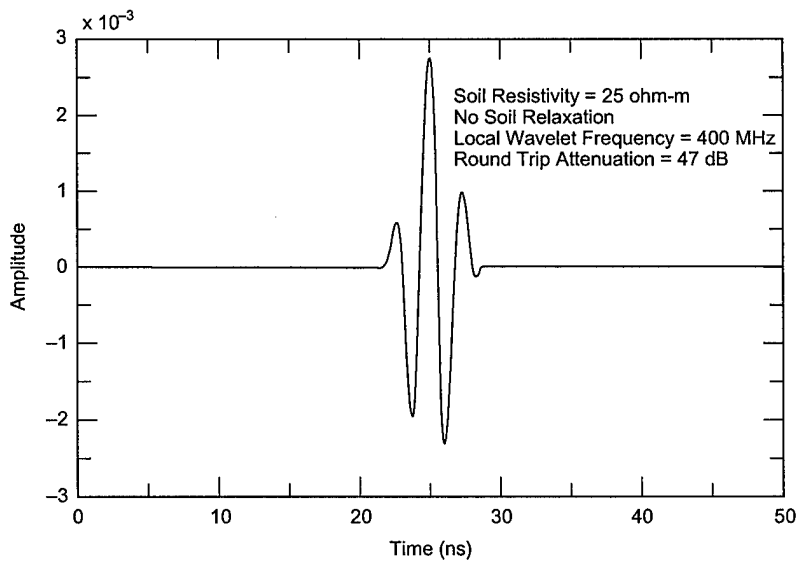

b. Reflections from purely resistive soils.

Figure 12 (cont'd). Model 400-MHz wavelets before and after round-trip propagation within 1 m of ground characterized by the soil parameters measured. The wavelets reflect from an interface for which R = –1 (eq. 6), which only reverses the phase of the wavelets so that all wavelet distortion and attenuation are due to propagation.

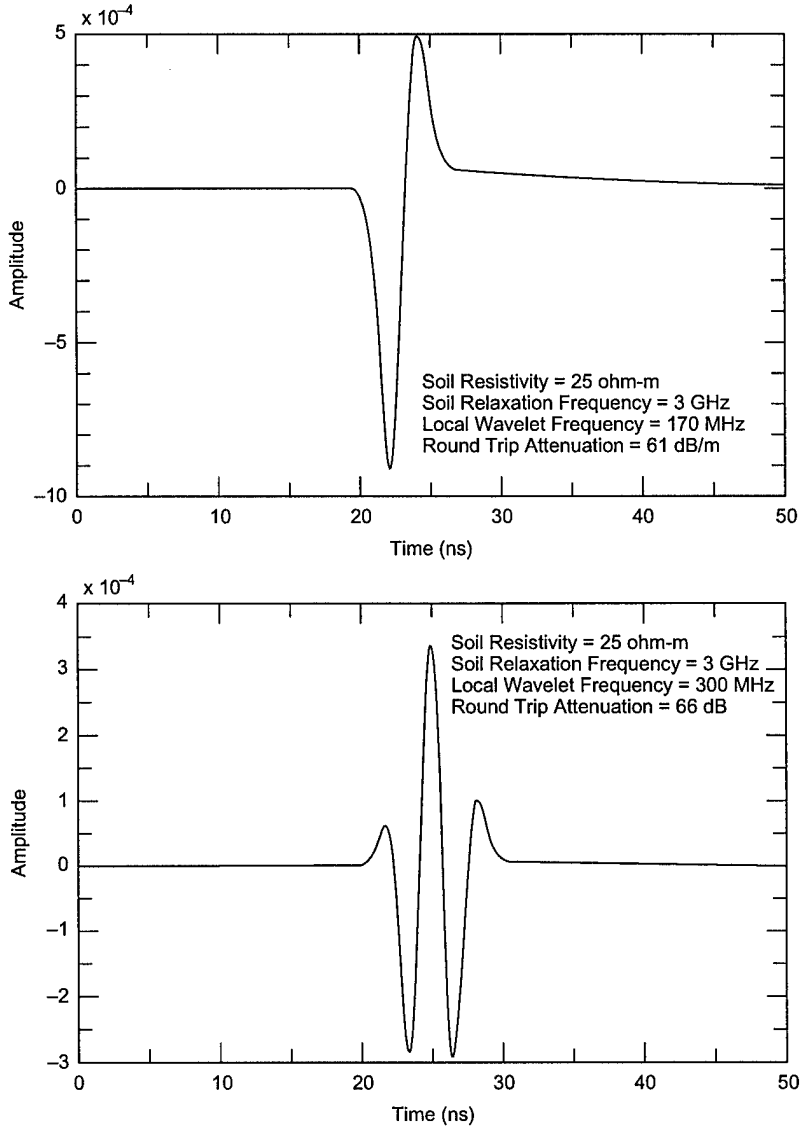

c. Reflections from resistive soil with dielectric relaxation at 3 GHz.

Figure 12 (cont'd).

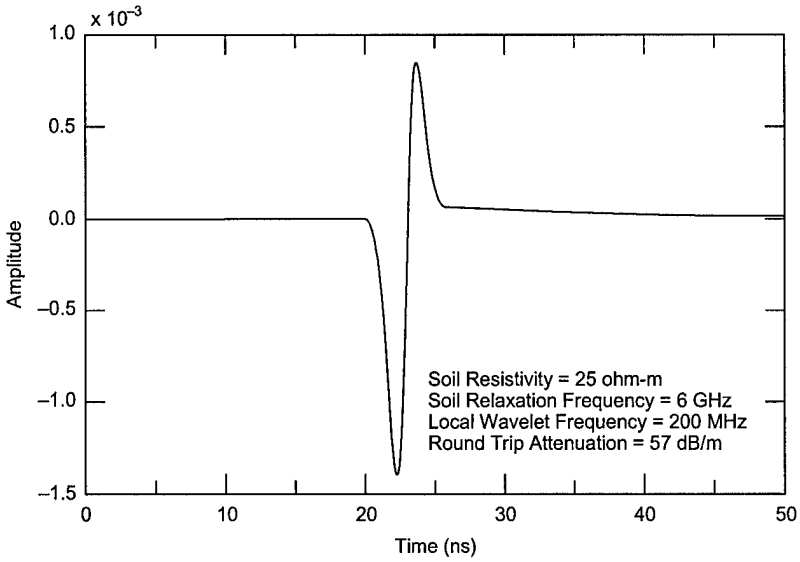

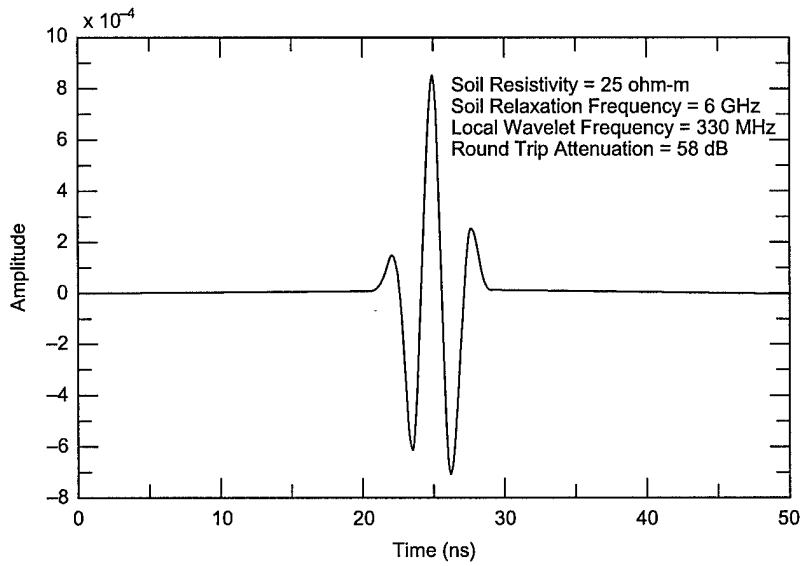

d. Reflections from resistive soil with dielectric relaxation at 6 GHz.

Figure 12 (cont'd). Model 400-MHz wavelets before and after round-trip propagation within 1 m of ground characterized by the soil parameters measured. The wavelets reflect from an interface for which R = –1 (eq. 6), which only reverses the phase of the wavelets so that all wavelet distortion and attenuation are due to propagation.

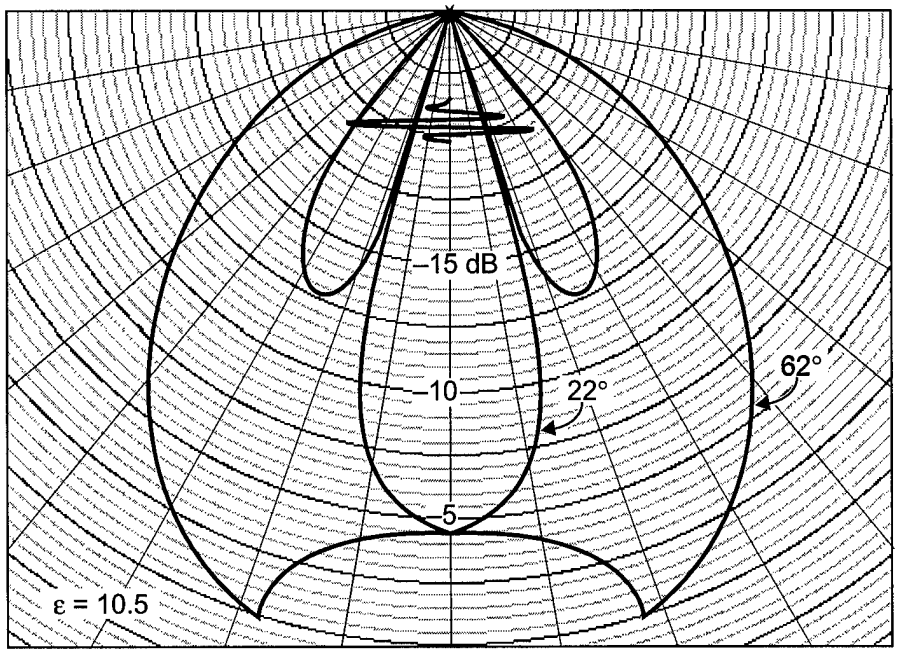

Figure 13. Radiation beamwidths for a model of our antennas and the average ε′ = 10.4 found at JPG. The solid curve is the beam pattern within the plane of the transect and is perpendicular to the direction of antenna polarization. The dotted curve is the beam pattern in the plane of the antenna polarization, which is perpendicular to the transect direction. Individual pattern 3-dB beamwidths are indicated at the point of the arrows. A typical form of the radiated wavelet is also shown. The curves assume that the transmitter and receiver antennas are coincident. They are actually spaced about 15 cm apart in the 300-MHz unit and slightly less in the 600-MHz unit.

ting antenna, we consider electric currents over the surface of a perfect electric conductor (PEC), where the tangential electric field E is negligible. In terms of integrals over the metal surface S,

$$\alpha(\mathbf{r})\mathbf{E}(\mathbf{r}) = \iint_S dS' \left\{ -\, i\omega\mu\; g(\mathbf{r},\mathbf{r}')\mathbf{J}(\mathbf{r}') + \frac{i\omega\mu}{k^2}\nabla\nabla g(\mathbf{r},\mathbf{r}')\cdot\mathbf{J}(\mathbf{r}') \right\} - \mathbf{E}(\mathbf{r})^{inc} \qquad (7)$$

$$\alpha(\mathbf{r})\mathbf{H}(\mathbf{r}) = \iint_S dS' \;\nabla g(\mathbf{r},\mathbf{r}')\times\mathbf{J}(\mathbf{r}') - \mathbf{H}(\mathbf{r})^{inc}$$

where $\mathbf{r}$ and $\mathbf{r}'$ are observation and integration field points, respectively; μ is the magnetic permeability of the soil, taken here to be that of free space ($4\pi \times 10^{-7}$ H/m); k is the electromagnetic wavenumber (m^{-1}); and $\mathbf{E}$ (V/m) and $\mathbf{H}$ (A/m) are the radiated electric and magnetic fields, respectively. The quantity α is a geometrical factor equal to the solid angle subtended by the surface required to exclude the singularity when $\mathbf{r}$ equals $\mathbf{r}'$, divided by 4π. Thus at a point on a smooth, i.e., locally flat surface, α is one-half. The surface currents $\mathbf{J}$ are equal to $\hat{\mathbf{n}} \times \mathbf{H}$, where the unit normal vector $\hat{\mathbf{n}}$ points outward from the surface, while the tangential electric field, proportional to $\hat{\mathbf{n}} \times \mathbf{E}$, has been considered negligible (perfect conductor). The scalar Green function g is

$$g = \frac{e^{ikR}}{4\pi R}, \qquad R \equiv |\mathbf{r} - \mathbf{r}'| \,. \qquad (8)$$

Taking the vector cross product of $\hat{\mathbf{n}}$ with equation (7) for $\mathbf{H}$ leads to

$$\alpha(\mathbf{r})\mathbf{J}(\mathbf{r}) - \iint_S dS' \left\{ \left(\hat{\mathbf{n}}(\mathbf{r})\cdot\mathbf{J}(\mathbf{r}')\right)\nabla g(\mathbf{r},\mathbf{r}') - \mathbf{J}(\mathbf{r}')\left(\hat{\mathbf{n}}(\mathbf{r})\cdot\nabla g(\mathbf{r},\mathbf{r}')\right) \right\} = \hat{\mathbf{n}}(\mathbf{r})\times\mathbf{H}(\mathbf{r})^{inc} \,. \qquad (9)$$

We approximate the target geometry using N surface elements, each being a flat triangular facet. To achieve the numerical formulation we assume further that the current **J** is approximately constant over each such element, associating its value with the location of the element's centroid, $\mathbf{r}_i$, i.e., $\mathbf{J}_i = \mathbf{J}(\mathbf{r}_i)$ for the ith element. Locating **r** only at the centroid of each element means that what follows α is always one-half. Altogether we obtain

$$\tfrac{1}{2}\mathbf{J}_i - \iint_{\Sigma S_j} dS' \left\{ \left(\hat{\mathbf{n}}_i \cdot \mathbf{J}_j\right) \nabla g(\mathbf{r}_i, \mathbf{r}') - \mathbf{J}_j \frac{\partial g}{\partial n_i}(\mathbf{r}_i, \mathbf{r}') \right\} = \hat{\mathbf{n}}_i \times \mathbf{H}_i^{inc} \tag{10}$$

where S_j is the area of the jth element. Thus over each element we need only evaluate the integral

$$Vp_{ij} = \iint_{S_i} dS' \frac{\partial g}{\partial p_i}, p = s, t, n \tag{11}$$

where s and t are locally constructed tangential coordinates, and n is the local outward normal coordinate. We used four-point Gaussian quadrature to ensure accuracy in this integration.

Locating $\mathbf{r}_i$ at each element centroid in succession provides N vector equations in the N unknown current elements $\mathbf{J}_i$. These currents are tangential to the surface. Expressing the ultimate governing relations in terms of tangential s and t components we obtain

$$\begin{aligned} &\tfrac{1}{2}\mathbf{J}_{si} - \sum_j \left[\left(\hat{\mathbf{n}}_i \cdot \hat{\mathbf{s}}_j\right) Vs_{ij} + \left(\hat{\mathbf{s}}_i \cdot \hat{\mathbf{s}}_j\right) Vn_{ij} \right] \mathbf{J}_{sj} - \\ &\sum_j \left[\left(\hat{\mathbf{n}}_i \cdot \hat{\mathbf{t}}_j\right) Vs_{ij} + \left(\hat{\mathbf{s}}_i \cdot \hat{\mathbf{t}}_j\right) Vn_{ij} \right] \mathbf{J}_{tj} = \\ &- \hat{\mathbf{t}}_i \cdot \mathbf{H}_i^{inc} \tfrac{1}{2}\mathbf{J}_{ti} - \sum_j \left[\left(\hat{\mathbf{n}}_i \cdot \hat{\mathbf{s}}_j\right) Vt_{ij} + \left(\hat{\mathbf{t}}_i \cdot \hat{\mathbf{s}}_j\right) Vn_{ij} \right] \mathbf{J}_{sj} - \sum_j \left[\left(\hat{\mathbf{n}}_i \cdot \hat{\mathbf{t}}_j\right) Vt_{ij} + \left(\hat{\mathbf{t}}_i \cdot \hat{\mathbf{t}}_j\right) Vn_{ij} \right] \mathbf{J}_{tj} = \hat{\mathbf{s}}_i \cdot \mathbf{H}_i^{inc} \ . \end{aligned} \tag{12}$$

This is the algebraic system to be solved. In effect, the method consists of applying point matching over a PEC, with pulse basis functions.

This formulation was chosen in part for its simplicity and hence programming convenience. Because tangential electric field components drop out, the initial governing equation is reduced at the outset. Associating the degrees of freedom with element centroids and locating observation points there cause all "self element" singularities to drop out of computations: in all self element integrations

$$\left(\hat{\mathbf{n}}_i \cdot \mathbf{J}_j\right) = 0 = \frac{\partial g}{\partial n_i}. \tag{13}$$

Once the currents are obtained from solution of the above algebraic system (12) they can be substituted in the equivalent of (7), expressed numerically in a manner similar to (12), to obtain scattered E and H fields at any observation point. In line with the assumptions outlined above, we calculate the (re)radiated fields, ignoring the influence of the ground surface discontinuity, i.e., as if the radiating currents were in an infinite soil medium. The computer program was tested against detailed near-field solutions for cases where analytical solutions are available (sphere), and against reasonableness checks for signal loss as a function of distance within the soil.

INCIDENT FIELD AND POLARIZATION PARAMETERS

The basic setup assumed for the antenna-target system is shown in Figure 14. The antenna is simulated by a sheet of currents deemed to be a reasonable approximation of those on a metal surface driven as a dipole antenna. We adjusted this current distribution so that its subsurface radiation pattern resembles patterns considered representative of those from a dipole antenna resting on a ground surface. To accomplish this, the antenna current distributions are expressed as

$$\mathbf{J}(y,z) = \hat{\mathbf{y}} \cos\left(\left(z - z_a\right) \big/ \pi w_z \right), \quad |y - y_a| \le w_y, |z - z_a| \le w_z \tag{14}$$

where $w_y = 0.8$ m and $w_z = 0.4$ m. In choosing unit value maximum current magnitude, we implicitly normalize all simulations with respect to that dimension of input. In their general features, i.e., 3-dB beamwidth, lobe patterns, and angular locations where the fields decline rapidly towards minima, patterns from these distributions fit our needs here.

Our antenna model thus consists of a rigorous representation of a synthetic or idealized structure. The resulting fields are strictly in accordance with Maxwell's

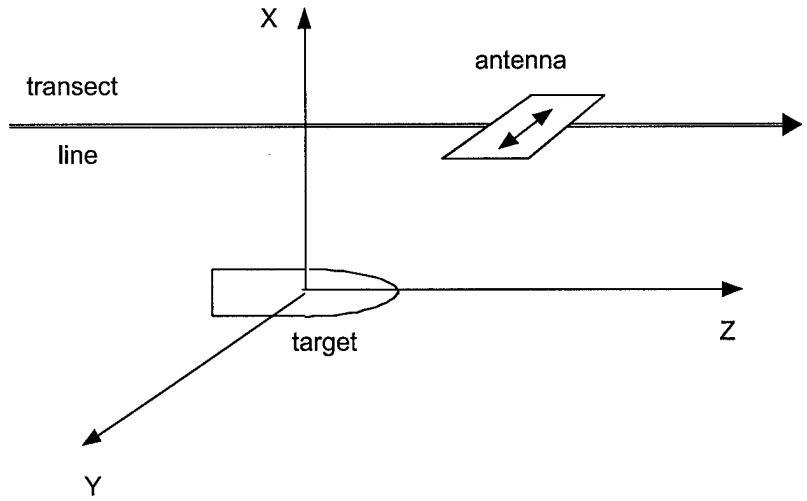

Figure 14. Basic setup, with target below ground surface, in its reference orientation. The fully polarimetric, orientable antenna is above it, at some position on a survey transect line.

equations, which underlie Huygen's principle and form the basis for describing all electromagnetic wave phenomena. Any input to our problem that violates those equations to some degree thwarts our ability to check the ultimate output for electromagnetic consistency, e.g., energy conservation. Beyond this, the antenna model contains two basic features in common with the actual antennas in frequent use: broader, smoother pattern in the H plane, which is usually coincident with the survey transect direction; and beamwidth that depends on frequency in the manner of a current sheet or set of aperture fields. In practice, numerical computation of the incident H values at each element centroid was a very minor burden, in terms of both programming and CPU time.

Because the fields radiated by the antenna are not planar, we will indicate antenna orientation rather than speak of the polarization of the incident field. We always assume that currents run in its long direction with the same distribution relative to the antenna. Especially because we are surveying at shallow depths, the incident field is nonuniform in both magnitude and direction over the target geometry. In practice, the orientation of the E field over most of the target is reliably in the E plane of the antenna. In the (x,z) plane, which contains the transect line, the most consistent E field orientation results from the reference antenna orientation in Figure 14: the transmitted E field is always normal to that plane, parallel to the Y axis. For received signals we assume that a horizontally oriented antenna records the computed E_y and E_z, without applying the antenna pattern to its receiving characteristics.

MODELING RESULTS

In what follows, the survey transect is always 0.7 m above the target, as if along a ground surface. We sometimes consider cases in which the antenna is variously rotated relative to the target axis or relative to the transect direction. The latter rotation was not enlisted systematically in the field measurements at JPG discussed here. However, it offers insight into possible target scattering behavior when the target is arbitrarily oriented relative to the incident field, which was likely to be the case during a survey. Some of the features in the field profiles push questions to the fore: how can the target response from points not above the target arrive relatively early in time, then appear to fade somewhat, then return to higher amplitude? Rotations of the target relative to the antenna are seen below to impose interesting spatially and frequency dependent patterns in the scattered signal. Relative rotation of antenna and target also suggest ways of discriminating hard cases.

First we examine scattering responses when the projectile is level, beginning with it oriented in the Y direction ($\theta_d = 0$ = declination; $\theta_x = 90°$ = horizontal

rotation about X axis, relative to reference target orientation). In this case, given the reference antenna orientation (Fig. 14), the incident E field is aligned with the target. Although the same effects described below are generally apparent without normalization, for generality we scale the magnitude of the received signal by the magnitude of the incident field at the target, E_o, as a function of frequency. Figure 15 shows normalized backscatter response across the band. The clear maximum occurs at 100 MHz where, given the dielectric constant assumed ($10.2 + i\,2.8 \times 10^{-3}$), the subsurface wavelength is almost exactly twice the target length. That is, the projectile responds most strongly when it can serve as a half-wavelength dipole antenna. The change in the target's cross-sectional shape along its axis does not appear to interfere significantly with this effect.

Perhaps more revealing than this horizontal case, similar scattering behavior is apparent when the target is inclined further, even when it is rotated about the vertical (x) axis. The lower (solid) line in Figure 15 shows the effect of adding a 45° inclination (θ_d) to the target, keeping it in (x,y) plane. We see a clear succession of higher modes for higher multiples of $L/(\lambda/2)$. This pattern persists for a variety of inclinations and rotations (Fig. 16), as long as the impinging radiation travels longitudinally along the surface of the target to some degree. Here the "total" scattered field magnitude E_{tot} is defined as $\sqrt{|E_y|^2 + |E_z|^2}$. Rotating the target back towards the reference orientation ($\theta_x = 0°$) and deepening its inclination diminishes the first, lowest mode and brings out the higher modes, ultimately more strongly than the first. Given the dielectric constant, this kind of pattern allows one to infer the target length from the separation of the peaks/troughs in the pattern. Previous investigators (Geng et al. 1999) have demonstrated the existence of shape-dependent natural resonant modes in currents in, and associated radiation from, metallic bodies of revolution (BORs). These correspond to electromagnetic "free vibration," after any forcing effects have died out, at frequencies less than 1 MHz, consisting primarily of decay patterns. Here we see what are in many ways comparable effects in the radar frequency range, when responses are forced and the resonant frequencies we seek are real valued.

As $\theta_x \Rightarrow 0$ we lose the kind of amplitude pattern in the previous two figures, but fortunately we gain another, which adds basic information as long as $\theta_d < 90°$. The upper line in Figure 17 shows the normalized scattered E field magnitude when the antenna is directly above a level projectile ($Z_a = 0$). Both antenna and target are in the reference configuration (Fig. 14). The lower line shows results for the same case but with the projectile inclined 45° ($\theta_d = 45°$, $\theta_x = 0$) and the antenna is located at $Z_a = 0.72$. Both results are shown vs. Re{k}a where a is the radius of the uniformly cylindrical portion of the target. Basically, both of these show most of the first cycle in the well-established cyclical scattering cross-section pattern for a circular cylinder, in the resonance region, under normal incidence with transverse E field (Bowman et al. 1988).

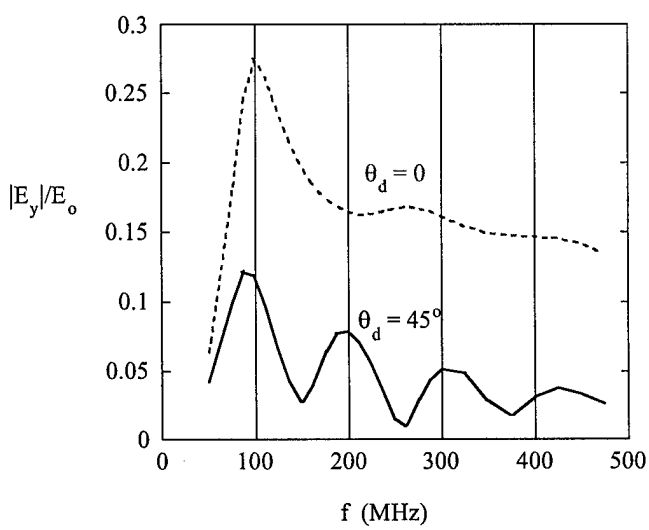

Figure 15. Normalized scattered electric field above a projectile surrounded by soil and oriented in the Y direction, as a function of frequency.

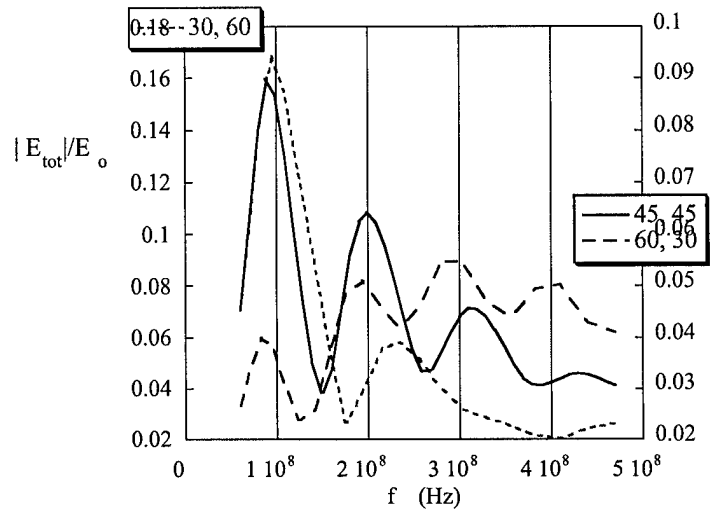

Figure 16. Normalized scattered E field above target for various projectile inclinations and rotations θ_d, θ_x.

The peak in the curve occurs at the *ka* value one would expect for an infinitely long circular cylinder with radius *a*, when creeping waves around the target interfere constructively with direct backscatter from the front of the target. Thus a plot of results for this target orientation implicitly reveals the value of *a*. We note that the tapering down of target cross section into its nose does not seem to affect these results, i.e., *a* refers to the radius of the uniform section of the target cylinder.

The appearance of resonance peaks in the patterns can provide essential information about target geometry. But they can also lead the surveyor astray. The positions where these peaks appear depend both on frequency and vantage point. Thus, for example, low frequencies coming from an antenna to the side of the target (the low-frequency portion of the incident beam is wider than the higher frequency) could provoke strong peaks. However, when the antenna has been moved,

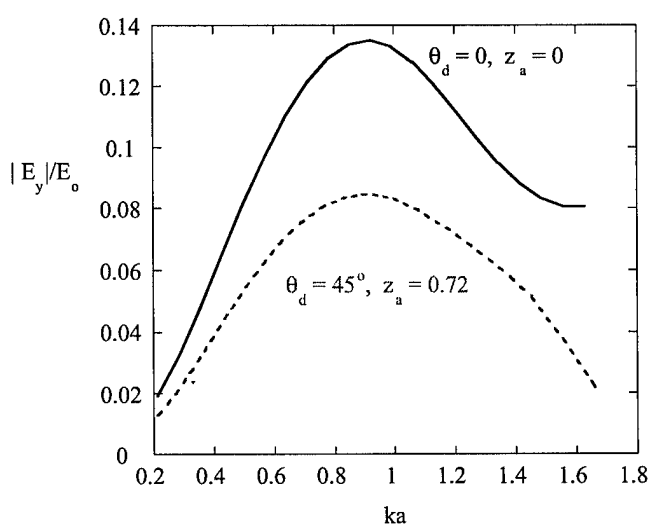

Figure 17. Normalized scattered E field when projectile axis is in (x,z) plane, from different vantage points Z_a, with different declinations θ_d.

different frequency content in the beam and different incidence angles would cause different responses to become relatively more prominent. A key to successful discrimination will be to identify various target characteristics in stages, starting with things like depth and orientation, and then use these to calibrate subsequent treatment of the data.

Examination of the broadband response along the transect can reinforce the above target length estimation, while adding information about the variation of its geometry along its axis. Figure 18 shows backscattered E_z amplitudes along the transect when the projectile is inclined at 45° with its nose up (i.e., $\theta_d = 225°$, $\theta_x = 0$). This orientation does indeed occur in reality, though it is less common than a nose-down subsurface rotation. In any case, our purpose here is primarily to study the fundamental effects of target orientation, whatever it may be. In this and all subsequent figures, scattered field values are not normalized. To provide the most general illumination, the antenna has been rotated horizontally 45° so its axis is oblique to the transect direction, producing an incident E field neither aligned with nor transverse to the target axis. In practice this can be accomplished by two measurements, one with parallel and the other with perpendicular antenna orientation; these results can then be combined for a completely general polarimetric characterization.

Figure 18 shows a progression over increasing frequency, from more or less a single event (peak) at 100 MHz, through two and three events at 200 MHz and 300 MHz, respectively, and four events at 400 MHz. That is, the number of peaks/events corresponds to the number of half wavelength multiples in the target length. In this case, the E_z backscattered field component is generated by the tendency of the target to induce currents preferentially in the general direction of its long axis. In fully polarimetric surveying, this tendency, together with the circumferential creeping wave phenomena illustrated in Figure 17, produces characteristic and very revealing induced ellipticity and depolarization in the scattered signals (O'Neill et al. 1999).

The pattern in Figure 18 is altered in certain interesting details when the projectile direction is reversed, that is, with the same overall orientation but with its nose down and tail up ($\theta_d = 45°$, $\theta_x = 0$). Figure 19 shows backscattered E_z magnitudes for this case. It is evident that the upward pointing flattened end of the target has a prominent influence in changing the pat-

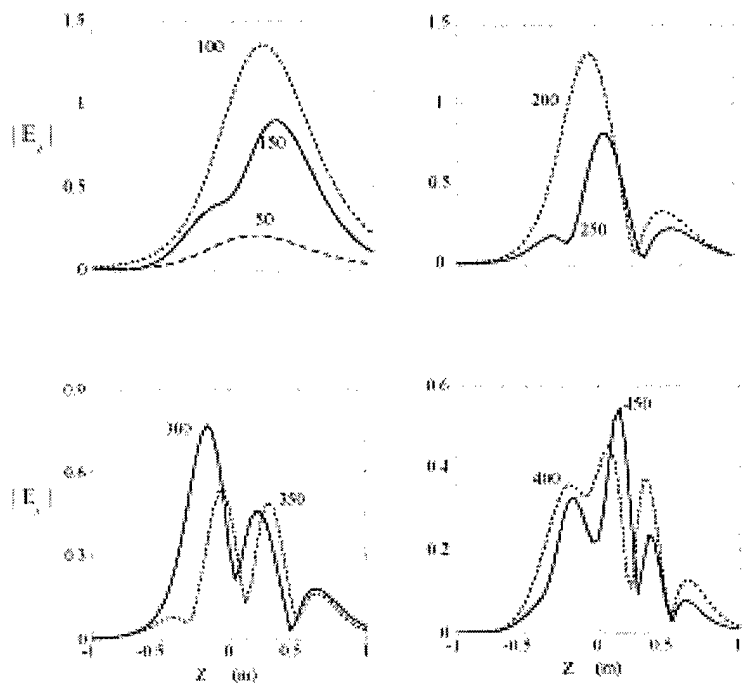

Figure 18. Backscattered E_z field magnitudes along transect, at various frequencies, when the projectile is inclined at 45° with nose up ($\theta_d = 225°$, $\theta_x = 0$), and the antenna is rotated $\theta_a = 45°$.

terns relative to those in the previous figure. In this nose-down case, increasing the frequency causes the scattering lobes to coalesce into smaller events on one larger background lobe, shifted towards $Z_a < 0$. This is even more evident relative to the nose-up case when the E_y component is examined as well. This background lobe occurs in the range of Z_a when the incident radiation impinges most directly on the flattened target end. At the same time, we must note that this end orientation effect is not solely due to localized reactions induced on the flattened end itself. The dramatic rise of the backscatter for $Z_a < 0$ at frequencies corresponding to integral numbers of $L/(\lambda/2)$ indicates that this signal magnitude enhancement involves the current pattern down the entire length of the target.

Overall, in this set of examples we note that there are dramatic shifts in the magnitude of the response, depending on which frequencies come to the fore. We also note that the strongest response is sometimes shifted spatially off to the side of the target location, depending on its orientation.

In conclusion, we show three bistatic scattered field values ($|E_z|$) over the (x,z) cutting plane, for an inclined projectile. They were obtained from 3-D finite element simulations, at the single frequency of 150 MHz, including soil properties as specified above but adding a ground surface. That is, the material below the X = 0 has the aforementioned electrical properties, while that above it has the electromagnetic characteristics of free space.

Figure 20 shows bistatic scattering patterns for incidence at subsurface angles of 45°, zero, and –45° relative to the vertical axis, where negative incidence angles are taken to be in the *first* quadrant (positive x and z). Analysis based on Fresnel coefficients and superposition of multiple reflections explains some apparently baffling features in the total scattered field shown: as the wave initially reflected from the target strikes the underside of the ground surface, it reflects back downwards. This downwards reflection interferes constructively with the upgoing component; that is, it does not change sign on reflection. This means that we see values of $|E_z|$ *increase* near the ground surface. We also see an overall pattern of two minima and two maxima along certain lines between the target and the surface. This is basically a standing wave interference pattern between upgoing and downgoing waves, and possible examples of this were seen in Figure 7 for transects G

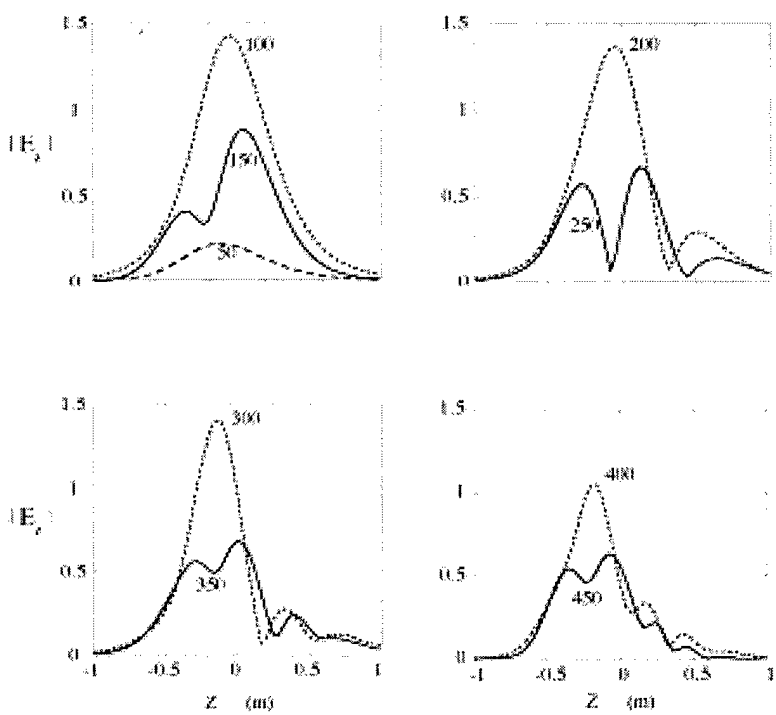

Figure 19. Backscattered E_z field magnitudes along transect, at various frequencies, when the projectile is inclined at 45° with nose down (θ_d = 45°, θ_x = 0), and the antenna is rotated θ_a = 45°.

and L where the target appeared to be near the surface. Most strikingly, the direction along which the strongest portions of the scattered field appear does not always run through the (mono-static, backscatter) observation point; or it does so, but not when the antenna is directly over the center of the target. Thus these simulations illuminate the ways in which interference patterns and directional biases in the signal, dependent on surface location and target inclination, can produce deceptive returns on the surface.

CONCLUSIONS AND RECOMMENDATIONS

Soil attenuation at JPG was extremely high, as evidenced by the high amount of gain required to display the signals received from within only the first meter of depth. The gain values of 50–65 dB that we applied are consistent with the general values of round-trip attenuation for 1 m of depth predicted by our propagation models. GPR bandwidths should be centered no higher than 600 MHz because the round-trip attenuation per meter of depth above this frequency may exceed the dynamic range of the radar. This fact precludes the use of any microwave system for detection of UXO. These high attenuation rates also greatly reduce off-axis sensitivity to targets so that full-diffraction signatures are rarely seen. We therefore recommend that the antenna towing speeds be kept very slow and data acquisition rates very high to ensure recording of as much of the diffraction responses as possible. We further recommend that an all-digital system eventually be developed so that extremely high rates (e.g., 512–1024 traces/s) would further allow noise reduction by trace stacking.

The most likely range of soil dielectric constants (5–14) is consistent with the measured moisture contents. The average value of about 10 predicts a narrow beamwidth in the plane parallel with the antenna polarization axis. This means that for normal towing operations, wherein the antennas are polarized perpendicular to the transect direction, the system is sensitive to ground mainly beneath the antennas. We therefore recommend that coverage be increased by using a multichannel radar system. Such operation is standard with present commercial systems, but its implementation compromises the data acquisition rate. Therefore, this is further reason for development of a real-time digitizing GPR system above 300 MHz that could acquire data at 512–1024 traces/s.

Horizontal filtering, normally an effective means of

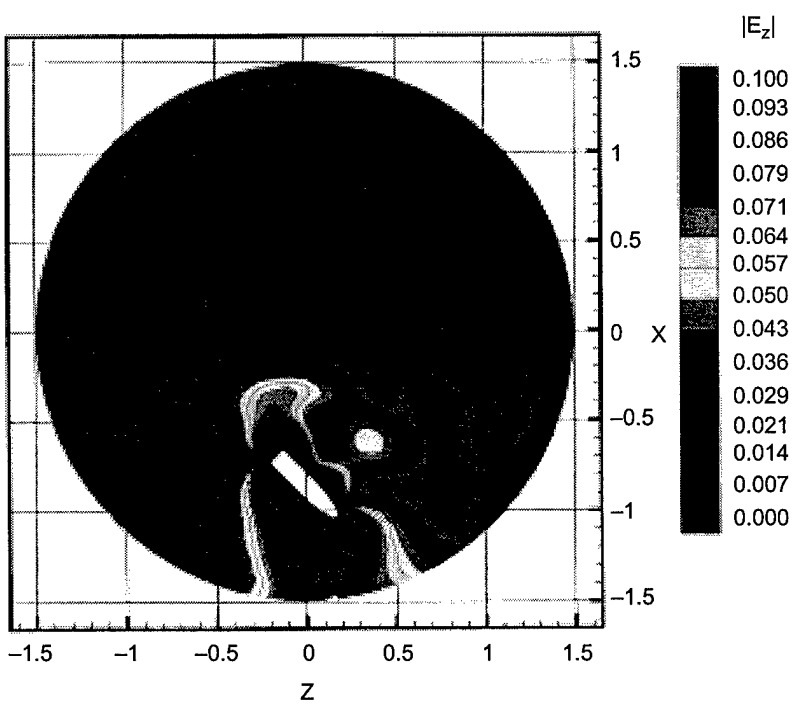

a. 45° from the left.

Figure 20. Scattered $|E_z|$ values, when the incidence direction and incident E field orientations are in the (x,z) plane, for various incidence angles.

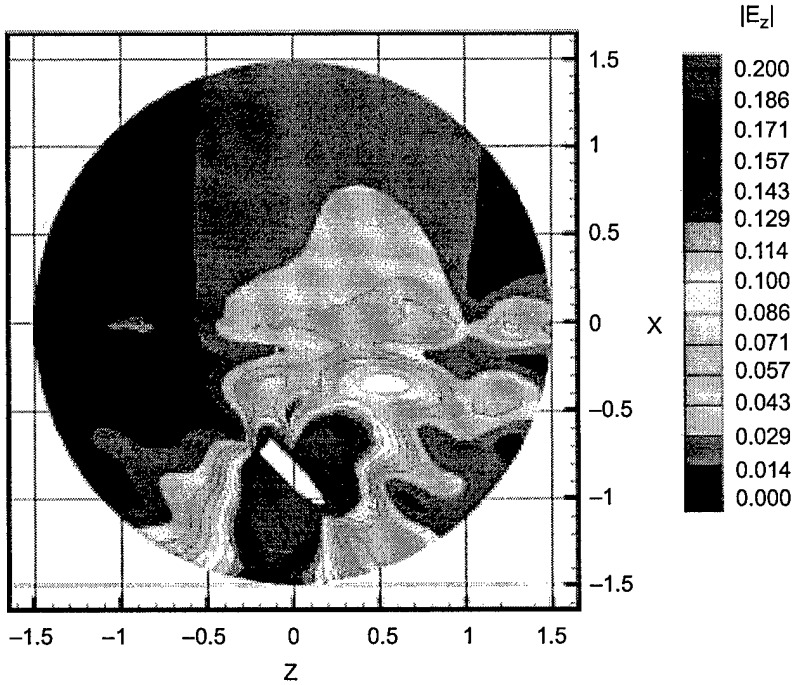

b. Vertical.

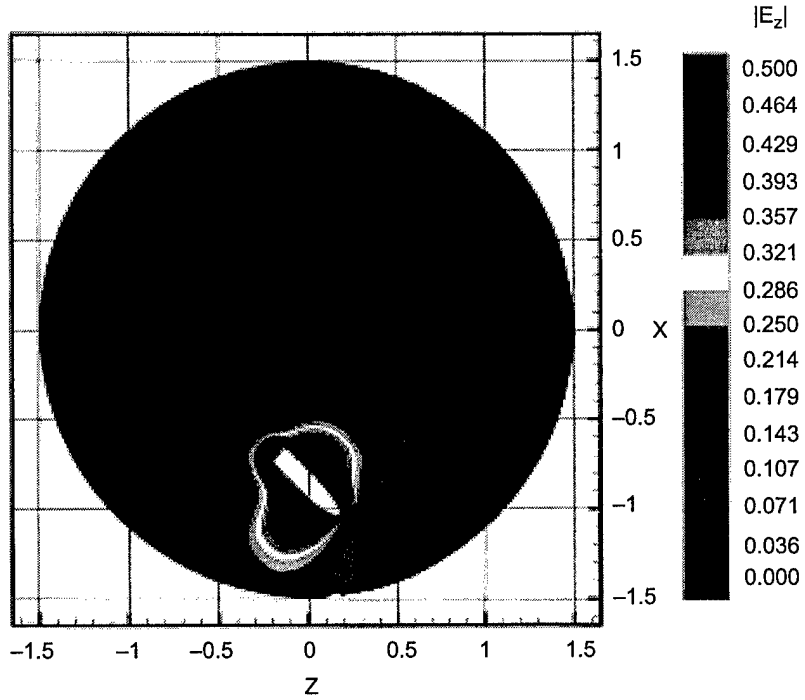

c. –45° (from 45° to the right of the vertical).

Figure 20 (cont'd).

reducing weak internal and external noise (or clutter) that occurs at constant time delay, was only partially successful. We have ascribed this result to the effects of uneven towing speeds and erratic contact between the ground surface and antenna faces upon antenna leakage. We recommend that a simple antenna platform, consisting of a heavy, high-density polyethylene "boat," be used to contain the antenna. The prow of the boat would help to deflect vegetation, and the weight would improve ground contact. The dielectric permittivity of the material is intermediate between air and ground and may improve the antenna impedance match with the near surface. The use of this platform may make the amplitude of the clutter bands more uniform and subject to better removal with horizontal filters.

We recommend that improved jitter control be specified in the design of future transmitters and receivers. Jitter is the slight shift in time that occurs in signal position from trace to trace. Although jitter may be only 1–2 ns, its reduction could significantly reduce noise when the trace length is only 30–50 ns.

We recommend that antennas for UXO detection remain on the surface. Airborne profiling, even at minimal heights of a few tens of centimeters, introduces an extra dielectric layer (air) into the propagation medium. In airborne profiling, returns from uneven subsurface interfaces will be strongly refracted along the surface and not be received because the value of $\varepsilon' = 1$ for air contrasts sharply with the ε' of the soil.

The wavelet shape transmitted by present, commercially available systems is probably most practical. Our theoretical studies show that shorter pulse length, which may be available with unshielded antennas, may shift too much in local frequency to be detected after propagation.

Future surveys should address the problem of total soil saturation. Our surveys were conducted in early fall, by which time these soils are usually below saturation. However, saturation levels are usually reached by late winter and can persist into late spring. Saturated soils have higher values of ε_s^* and f_{rel} and may therefore offer less attenuation per meter at 300–600 MHz than would moist soils. However, mechanical operation in mud may be a serious mobility problem.

EMI systems have shown themselves to be quite successful at UXO detection, even in site conditions that are unfavorable for GPR. At the same time, simulations show the distinct possibility that GPR may reveal key target characteristics, such as length and diameter. This suggests that more such simulation should be done and integrated into signal interpretation, and that the most important offering of GPR may be in the realm of discrimination more than UXO detection. Fully polarimetric GPR is both possible and potentially advantageous.

LITERATURE CITED

Arcone, S.A. (1995) Numerical studies of the radiation patterns of resistively loaded dipoles. *Journal of Applied Geophysics*, **33:** 39–52.

Arcone, S.A., D.E. Lawson, A.J. Delaney, J.C. Strasser, and J.D. Strasser (in prep) Ground-penetrating radar reflection profiling of groundwater and bedrock in an area of discontinuous permafrost. *Geophysics*.

Bowman, J.J., T.B.A. Senior, and P.L.E. Uslenghi (Ed.) (1988) *Electromagnetic and Acoustic Scattering by Simple Shapes*. New York: Elsevier.

Brillouin, L. (1960) *Wave Propagation and Group Velocity*. New York: Academic Press.

Clarke, T.S., and C.R. Bentley (1994) High-resolution radar on Ice Stream B2, Antarctica: Measurements of electromagnetic wave speed in firn and strain history from buried crevasses. *Annals of Glaciology*, **20:** 153–159.

Debye, P. (1929) *Polar Molecules*. Mineola, New York: Dover Publications.

Delaney, A.J., and S.A. Arcone (1984) Dielectric measurements of frozen silt using time domain reflectometry. *Cold Regions Science and Technology*, **9:** 39–46.

Feynman, R.P., R.B. Leighton, and M. Sands (1964) *The Feynman Lectures on Physics, Vol. II*. Reading, Massachusetts: Addison Wesley Longman.

Geng, N., C.E. Baum, and L. Carin (1999) On the low-frequency natural response of conductivity and permeable targets. *IEEE Transactions on Geoscience and Remote Sensing*, **37**(1): 347–359.

Hoekstra, P., and A.J. Delaney (1974) Dielectric properties of soils at UHF and microwave frequencies. *Journal of Geophysical Research*, **79:** 1699–1708.

Hoekstra, P., and W.T. Doyle (1971) Dielectric relaxation of surface adsorbed water. *Journal of Colloid and Interface Science*, **36:** 513–521.

Jezek, K.C., C.R. Bentley, and J.W. Clough (1979) Electromagnetic sounding of bottom crevasses on the Ross Ice Shelf, Antarctica. *Journal of Glaciology*, **24:** 321–330.

Kong, J.A. (1990) *Electromagnetic Wave Theory*. New York: John Wiley and Sons.

Llopis, J.L. (in prep) Soil resistivity measurements at JPG. Engineer Research and Development Center, Vicksburg, Mississippi, Technical Report.

NAVEOD (1997) *Unexploded ordnance (UXO): An overview*. Naval Explosive Ordnance Disposal Technology Division, UXO Countermeasures Department, Indian Head, Maryland.

Nickell, A.K. (1985) *Soil Survey of Jefferson County, Indiana*. U.S. Department of Agriculture, Soil Conservation Service, 169 pp.

O'Neill, K., S.A. Haider, S. Geimer, and K.D. Paulsen (in prep) Effects of a proximate grounds surface on basic broadband polarimetric scattering from buried metallic targets. *IEEE*.

Parkhomenko, E.I. (1967) *Electrical Properties of Rocks*. New York: Plenum Press.

Péwé, T.L. (1955) Origin of the upland silt near Fairbanks, Alaska. *Geological Society of America Bulletin*, **67:** 699–724.

Rodbell, D.T., S.L. Forman, J. Pierson, and W.C. Lynn (1997) Stratigraphy and chronology of Mississippi Valley loess in western Tennessee. *Geological Society of America Bulletin*, **109:** 1134–1148.

Stratton, J. (1941) *Electromagnetic Theory*. New York: McGraw-Hill.

Tice, A.R., J.L. Oliphant, Y. Nakano, and T.F. Jenkins (1982) Relationship between the ice and unfrozen water phases in frozen soil as determined by pulsed nuclear magnetic resonance and physical desorption data. USA Cold Regions Research and Engineering Laboratory, CRREL Report 82-15.

Topp, G.C., J.L. Davis, and A.P. Annan (1980) Electromagnetic determination of soil water content: Measurements in coaxial transmission lines. *Water Resources Research*, **16:** 574–582.

Wait, J.R. (1955) Scattering of a plane wave from a circular dielectric cylinder at oblique incidence. *Canadian Journal of Physics*, **33:** 189–195.

Wait, J.R. (1970) *Electromagnetic waves in stratified media, 2nd Ed.* New York: Pergamon Press.

REPORT DOCUMENTATION PAGE

Form Approved
OMB No. 0704-0188

Public reporting burden for this collection of information is estimated to average 1 hour per response, including the time for reviewing instructions, searching existing data sources, gathering and maintaining the data needed, and completing and reviewing this collection of information. Send comments regarding this burden estimate or any other aspect of this collection of information, including suggestions for reducing this burden to Department of Defense, Washington Headquarters Services, Directorate for Information Operations and Reports (0704-0188), 1215 Jefferson Davis Highway, Suite 1204, Arlington, VA 22202-4302. Respondents should be aware that notwithstanding any other provision of law, no person shall be subject to any penalty for failing to comply with a collection of information if it does not display a currently valid OMB control number. PLEASE DO NOT RETURN YOUR FORM TO THE ABOVE ADDRESS.

1. REPORT DATE *(DD-MM-YY)*
April 2000

2. REPORT TYPE
Technical Report

3. DATES COVERED *(From - To)*

4. TITLE AND SUBTITLE
UXO Detection at Jefferson Proving Ground Using Ground-Penetrating Radar

5a. CONTRACT NUMBER

5b. GRANT NUMBER

5c. PROGRAM ELEMENT NUMBER

6. AUTHOR(S)
Steven A. Arcone, Kevin O'Neill, Allan J. Delaney,
and Paul V. Sellmann

5d. PROJECT NUMBER

5e. TASK NUMBER

5f. WORK UNIT NUMBER

7. PERFORMING ORGANIZATION NAME(S) AND ADDRESS(ES)
U.S. Army Engineer Research and Development Center
Cold Regions Research and Engineering Laboratory
72 Lyme Road
Hanover, New Hampshire 03755-1290

8. PERFORMING ORGANIZATION REPORT NUMBER
ERDC/CRREL Technical Report 00-5

9. SPONSORING/MONITORING AGENCY NAME(S) AND ADDRESS(ES)
U.S. Army Environmental Center
Aberdeen Proving Ground
Maryland

Office of the Chief of Engineers
Washington, DC 20314-1000

10. SPONSOR / MONITOR'S ACRONYM(S)

11. SPONSOR / MONITOR'S REPORT NUMBER(S)

12. DISTRIBUTION / AVAILABILITY STATEMENT
Approved for public release; distribution is unlimited.

Available from NTIS, Springfield, Virginia 22161.

13. SUPPLEMENTARY NOTES

14. ABSTRACT

Ground-penetrating radar (GPR) was used to detect UXO and nonordnance on the 40-acre site (lot 54) of Jefferson Proving Ground, Indiana. The UXO are buried about 1 m deep in a clayey silt for which the soil water content ranged from moist near the surface to near saturation at about 1 m. A 16-bit radar was used to profile along previously established lines and transects over emplaced artificial targets. Data were recorded at 48–64 traces/s with minimal towing speeds during both dry and rainy weather. Target responses at both 300 (time range of 50 ns) and 600 MHz (30 ns) ranged from discrete diffractions to short reflection segments. Soil loss greatly attenuated diffraction hyperbolas. Theoretical analyses of these hyperbolas give an average soil dielectric constant of 10 at both 300 and 600 MHz. The phase polarity of many of the reflected and diffracted wavelets indicate targets with wave impedances higher than that of the soil. It is therefore assumed that these targets are metallic and the responses of some, whose locations correlate with the position of UXO on burial maps, are shown in detail. Theoretical modeling of wavelet propagation for this soil confirms the high rate of attenuation (47–66 dB/m round-trip), the maintenance of waveform, a shift in wavelet local frequency, and response to a typical UXO. It is concluded that GPR is effective for finding targets in this type of soil to no more than 2-m depth. It is recommended that future surveys utilize high trace acquisition rates to capture the full target responses, and a prowed, heavy dielectric antenna sled to improve antenna-to-ground coupling and to deflect surface obstacles such as vegetation. Broadband, three-dimensional numerical modeling of scattering from UXO-shaped targets in soil, with diverse orientations of antenna and target relative to one another, suggests that target length and diameter may be inferred from resonance patterns in backscattered signals. The simulations also reveal some ways in which oblique target/antenna orientations along a transect may affect frequency-dependent response patterns, providing clues as to target shape as well as positional ambiguities.

15. SUBJECT TERMS
Dielectric constant
Ground-penetrating radar
Unexploded ordnance (UXO)

16. SECURITY CLASSIFICATION OF:			17. LIMITATION OF OF ABSTRACT	18. NUMBER OF PAGES	19a. NAME OF RESPONSIBLE PERSON
a. REPORT	b. ABSTRACT	c. THIS PAGE			19b. TELEPHONE NUMBER *(include area code)*
U	U	U	U	39	

Standard Form 298 (Rev. 8-98)
]Prescribed by ANSI Std. 239.18